Article

Au-Cu Resources in Some Mines from Antiquity in the South Gabal Um Monqul and Gabal Al Kharaza Prospects, North Eastern Desert, Egypt

Abdallah Atef [1],*, Adel A. Surour [1,2], Ahmed A. Madani [1] and Mokhles K. Azer [3]

[1] Department of Geology, Faculty of Science, Cairo University, Giza 12613, Egypt;
adelsurour@cu.edu.eg (A.A.S.); aamadani18@hotmail.com (A.A.M.)
[2] Department of Geological Sciences, Faculty of Science, Galala University, New Galala City 43511, Egypt
[3] Geological Sciences Department, National Research Centre, Giza 12622, Egypt; mokhles72@yahoo.com
* Correspondence: abdallah@sci.cu.edu.eg

Abstract: Since Antiquity, sustainable resources of gold and copper have been mined at two prominent prospects in the north Eastern Desert of Egypt, namely the south Gabel Um Monqul (SGUM) and Gabal Al Kharaza (GKZ). Mineralization is hosted by Neoproterozoic shield rocks represented by dacite and monzo- to syenogranite at the SGUM prospect whereas they are diorite, granodiorite, and quartz feldspar porphyry at the GKZ prospect. These hosts have been emplaced in an island arc environment from calc-alkaline magmas with a peraluminous to metaluminous signature. They are hydrothermally altered including albitization, sericitization, silicification, epidotization, and chloritization. The Au and Cu mineralizations are confined to shear zones that lately filled with auriferous quartz veins adjacent to mineralized alteration zones. In the GKZ prospect, the old trenches trend mainly in a NW–SE direction whereas it is NE–SW and NW–SE in the SGUM prospect. Evidence of shearing ranges from megascopic conjugate fractures and shear planes in the outcrops to microscopic sheared and crumbled Au-Cu ore assemblages dominated by Fe-Cu sulfides, specularite, and barite. Microscopic investigation suggests that the formation of specularite is due to the shearing of early existing magnetite. The ore textures and paragenetic sequence indicate that pyrite in the alteration zones is oxidized, leading to the liberation of gold up to 3.3 g/t. The formulae of the analyzed electrum lie in the range $Au_{74.5-76.8} Ag_{22.2-24.5}$. Integration of the field, geochemistry, and mineral chemistry data, combined with the gold fire assay data prove the presence of sustainable amounts of disseminated Au and Cu, not only in the mineralized quartz veins, but also in the alteration zones. Data materialized in our paper show similarities in the style of mineralization at the SGUM and the GKZ prospects with iron oxide-copper-gold (IOCG) deposits elsewhere in the Arabian-Nubian Shield (ANS) and other world examples.

Keywords: sustainable Au-Cu resources; alteration zone; shear zone; IOCG; north Eastern Desert; Egypt; Arabian-Nubian Shield

1. Introduction

The Precambrian basement rocks of Egypt constitute the northern part of the Nubian portion of the Arabian-Nubian Shield (ANS). The ANS is a part of the Pan-African orogenic belt that comprises a large area of northeast Africa and the Arabian Peninsula. The Neoroproterozoic crust of the ANS is formed by an accretionary orogenic belt between East and West Gondwana as the result of the closure of the Mozambique Ocean [1,2]. The opening of the Red Sea resulted in the separation of the Shield into two parts, namely the Nubian Shield in northeast Africa (including Egypt) and the Arabian shield in the western part of the Arabian Peninsula. The Eastern Desert of Egypt constitutes the northwest extension of the ANS.

Egypt is well-known as an area of gold-mining since the dawn of history. In spite of their methods and tools, the ancient Egyptians discovered and exploited more than 100 vein-type gold deposits and occurrences spread over the entire basement rocks of Egypt [3–6]. Records of gold production date back to the Pharaonic, from the pre-dynastic times until the New Kingdom, Greek-Ptolemaic-Roman-Byzantine times, Islamic times, and continued up to the 5th century [3]. Mostly, gold in the basement rocks of Egypt is linked spatially to shear zones and their associated quartz veins that formed during tectonic movement of the Pan-African orogeny [4–8]. Classification of gold-bearing quartz veins in the Eastern Desert [4,6,9,10] can be listed as the following auriferous veins: (1) hosted by metavolcano-sedimentary assemblage and the granitic country rocks, (2) allied with ultramafic rocks, (3) connected with possible porphyry copper deposits, (4) related to the contact between younger gabbros and younger granites, and (5) associated with anorogenic younger granites. Gold-bearing quartz veins in the Neoproterozoic basement rocks of the Eastern Desert of Egypt were the main targets of gold for ancient workers and investigators [4,6,9,10], but recently, gold-bearing alteration zones hosted in the structurally controlled shear zones are well-known type of gold deposits in the ANS [11–18]. The gold-hosting porphyry copper system is recorded in the ANS specifically at the south Eastern Desert (SED) and north Sudan [19–27]. Hydrothermal iron oxide copper gold (IOCG) deposits have a long history of major resources of economic metals such as iron, copper, gold, silver, and uranium [28–36]. These deposits have a few preservations in the ANS. However, some attempts have recorded IOCG deposits within the Neoproterozoic basement rocks of the ANS [27,37,38].

Most workers believe that the north Eastern Desert (NED) is not a province for gold mineralization in comparison to central Eastern Desert (CED) and SED. The CED and SED are dominated by ophiolitic ultramafics and younger gabbro in association with younger granites, which are favorable settings for gold mineralization [10].

The present study concerns the gold and copper mineralizations in the NED, particularly at two ancient mining sites, namely the South Gabal Um Monqul (SGUM) and Gabal Al Kharaza (GKZ) prospects. Some researchers have studied the mode of occurrence and genesis of gold and copper mineralizations at the SGUM prospect. The Au-Cu mineralization in this prospect is mainly confined to shear zones following a NE–SW trend and impregnated with ferruginous barite veins and quartz-calcite veins [39]. This prospect was interpreted to be an epithermal system that contains considerable gold contents (up to 0.42 wt%) in the sulfides [40]. Botros and Wetait [21] considered the SGUM prospect as a porphyry copper system and defined four main alteration assemblages as follows: (1) hydrothermal biotite (potassic), (2) quartz-sericite-pyrite (phyllic), (3) sericite-clay (phyllic-argillic), and a (4) chlorite-carbonates-epidote (propylitic) zone. Fletcher [38] related the gold and copper mineralizations at the SGUM prospect to typical IOCG deposits. Recent contributions have suggested that the source of the copper and gold mineralizations is associated with the iron oxide-rich Cu-Au porphyry system than the IOCG system [27]. Recent studies of the GKZ prospect [41] have determined the concentrations of gold and copper in the ancient mining activities in diorite, granodiorite, and quartz feldspar porphyry. Unlike SGUM, neither the information regarding the styles of gold and copper mineralizations of the GKZ prospect nor the geochemical characterizations of the host rocks were recorded. Therefore, this paper provides comprehensive geological, petrographical, mineralogical, and geochemical studies of the basement rocks and their associated alteration zones in order to provide constraints on (1) the paragenetic sequence of ore and gangue minerals in addition to the influence of hydrothermal alterations on the enrichment of Au-Cu mineralization in both the alteration zones and related quartz veins, (2) petrogenesis of the host rocks in terms of the magma type and tectonic setting, and (3) the ore genesis to present a reasonable genetic model(s) for the mineralizations type(s) at the SGUM and GKZ prospects. Unlike the SGUM prospect, this work can be considered as the first insightful work on the GKZ prospect.

2. Geologic Setting and Field Observations

Regionally, the area of study is located in the northern province of the Eastern Desert, specifically in the Ras Gharib segment (Figure 1a). In the Ras Gharib segment, a thick succession of basement rocks is present, comprising extrusive and intrusive rocks with a wide variation in lithology and age [21,27,42–46]. The Neoproterozoic basement rocks cropping out in the Ras Gharib segment represent one of the largest exposures of granitoid rocks in the NED. The Ras Gharib segment comprises two main rock suites, namely (a) the island arc suite (770–719 Ma) composed of metavolcanics, diorite, trondhjemites, and granodiorite, and (b) the post-collisional suite (630–590 Ma) consisting of Dokhan volcanics and their associated pyroclastics, Hammamat sediments, monzogranite to syenogranite, and alkali feldspar granite [42] (Figure 1b).
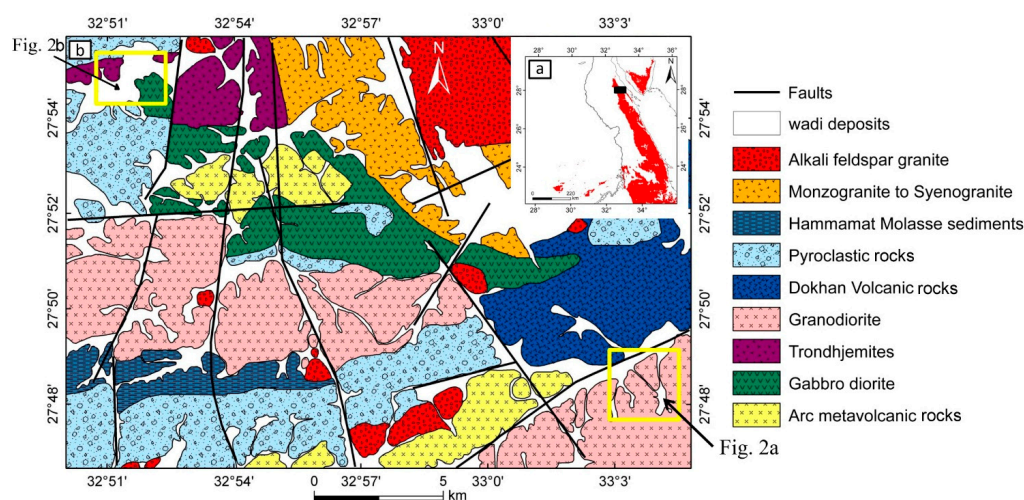

Figure 1. (**a**) Location map of the study area (black rectangle) showing the Nubian Shield rocks (red color). (**b**) Modified geological map of the Ras Gharib segment after [42]. The yellow rectangles define the locations of the SGUM and GKZ prospects.

The SGUM area (latitudes 27°47′40″ and 27°49′21″ N and longitudes 33°02′48″ and 33°05′38″ E) is located at the south of Gabal Um Monqul and consists mainly of younger gabbro, Dokhan volcanics, and younger granites (Figure 2a). The gabbro represents the oldest rock unit at SGUM. It occurs as small semi-circular masses at the western part of the SGUM (Figure 2a). Careful field studies have revealed that the gabbro is massive with no apparent layering or cumulate textures. Although this gabbro has a limited distribution and size, there is a clear relation and sharp contacts with the surrounding volcanic rocks. Unlike mineralizations hosted by the Dokhan volcanics and granitoid rocks, there was no observation of old trenches and dumbs around the gabbroic rocks. Detailed field investigations revealed that the Dokhan volcanics of the SGUM prospect have a gray color and occur as low to moderate peaks with pronounced porphyritic appearance in hand specimens. Dacite is dissected by a number of narrow shear zones with different trends. Mineralization is closely associated with hydrothermally altered volcanic rocks along shear zones. Some thick auriferous quartz veins and shafts for gold mining were observed along the shear zones (Figure 3a). The granitic rocks in the SGUM prospect comprise two main types, namely monzogranite and syenogranite. They are sometimes porphyritic, showing large plagioclase crystals. The granitic rocks exhibit very prominent features of chemical and mechanical weathering. These rocks are highly jointed and are characterized by conjugate fractures and exhibit some sort of spheroidal weathering. In the mineralized zone, the granitic rocks exhibit shearing along a set of shear zones. Some auriferous quartz veins and shafts for gold mining are present along the shear zones. The granitic rocks of the SGUM are dissected by numerous dikes (mafic and felsic dikes) with different compositions, trends, and thicknesses.

The GKZ prospect (latitudes 27°54′07″ and 27°55′8″ N and longitudes 32°50′44″ and 33°52′30″ E) is located in the Dara area and mainly comprises diorite, Dokhan volcanics, grandiorite, and quartz feldspar porphyries (Figure 2b). The diorite of the GKZ prospect is commonly massive and easily distinguished in the field from the surrounding rock by its gray color. The rock unit is subjected to a system of joints and fractures that are well-developed in different directions, but the NW–SE trend predominates. The joints are either vertical or sub-vertical. Diorite outcrops are dissected and traversed by a number of wide wadies that are filled with loose wadi deposits. Old excavations and open trenches with a range from 1 to 2 m are restricted to this rock unit. Sometimes, these trenches are cut by fault planes. The alteration zones, with black and reddish coloration, and related gold-bearing quartz veins are found associated with these trenches (Figure 3b). The older granitoids and quartz-feldspar porphyries of the GKZ prospect crop out at the northwestern part of the study area. Older granitoid is represented mainly by granodiorite whereas quartz feldspar porphyry is represented by dacite. These occur as small hills with gentle slopes. Both older granitoid and quartz-feldspar porphyry are well-jointed and the majority of joints follow the NW–SE direction (Figure 3c). The majority of joints are filled with secondary copper minerals and iron ores. Also, a large zone of auriferous quartz veins (mostly milky and less commonly smoky) can be observed. A huge volume of rock dumbs were left after the old mining works. Dumbs are rich in chrysocolla and black iron ores such as magnetite, specularite, and goethite, which surround the old excavations.
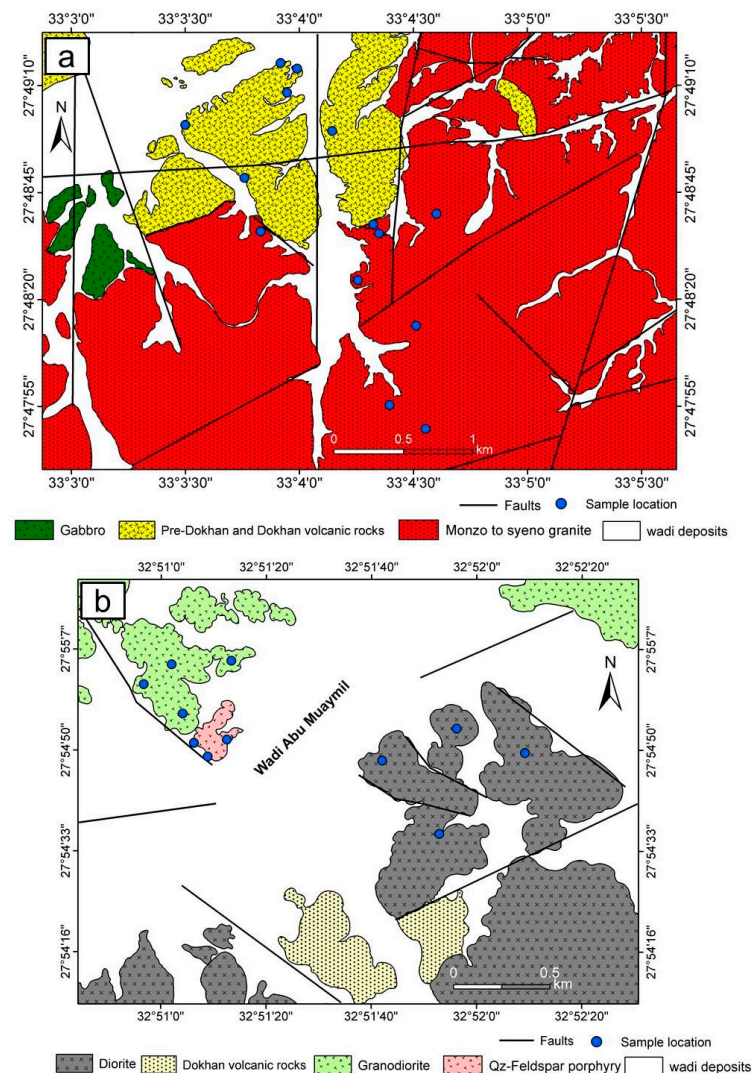

Figure 2. Geological maps of (**a**) the SGUM prospect and (**b**) the GKZ prospect.

Figure 3. (**a**) A shaft at the SGUM prospect confined to the shear zone in syenogranite (Sy); (**b**) alteration zone and sub-parallel quartz veins confined to the shear zone in granodiorite (Gr); (**c**) a set of joints follows a NW–SE direction in the sheared granodiorite (Gr).

3. Methods

During the field trip, representative specimens were carefully collected from fresh rocks, altered rocks, alteration zones, quartz veins, and dikes. Thin sections were prepared for the petrographic identification and description of different rock varieties under a polarized transmitted light microscope. A reflected light microscope was also used to identify opaque minerals, with a focus on the ore–gangue relationships and microfabrics of the mineralized rocks. Twenty-one representative samples covering the rock units in the area of study were selected and analyzed for major oxides, trace, and rare earth elements in order to identify their geochemical classification, magma type, and tectonic setting. The concentration of major, some trace, and rare earth elements were determined via combined X-ray fluorescence (ThermoARL XRF Spectrometer) and inductively coupled plasma (ICP) mass (Agilent7700ICP-MS) spectrometry (ICP-MS) at the GeoAnalytical Lab, Washington State University, USA. Major and trace elements were measured by the XRF technique through crushing and pulverizing each sample in an agate grinding bowl to obtain homogenous particles with a pebble size. The resulting sample was weighed, mixed with dilithium tetraborate flux, fused at 1000 °C in a muffle furnace, and cooled. The cooled bead was reground, refused, and polished via diamond laps to obtain a flat and smooth surface for analyses. The concentration of REE and some trace elements were analyzed using ICP-MS. For major oxide analyses, reference material 650CC from USGS standard rock powder GSP2 was used as standard whereas USGS (AGV-2 and RGM-2, DTS-2, BCR-1 and G-2) was used as the standard for REE and other trace elements measured by ICP-MS. The fire assay was used to determine the gold content in some representative mineralized samples. The analyses were carried out at the Central Laboratories of the Egyptian Mineral Resources Authority (EMRA) in Giza, Egypt. At the University of Nevada, Las Vegas, NY, USA, a JEOL jxa8900 electron microprobe was used to analyze the mineral chemistry of five polished thin slices. The polished thin sections were coated with 15 nm of amorphous carbon during the vacuum coater-assisted preparation technique for microprobe tests to make them conductive. Operating parameters included a beam diameter of 5–10 m, a count

time on peak of 30 s, a 15 kV accelerating voltage, and a beam current of 10 nA. An energy dispersive X-ray spectrometer (EDS) connected to a scanning electron microscope (SEM) type E SEM was used by the Nuclear Materials Authority of Egypt (NMA) to analyze the mineral chemistry of specific materials. The analytical parameters were 25–30 kV accelerating voltages, a beam resolution of 1–3 mm, and a counting time of 60–120 s.

4. Petrography

The gabbro of SGUM is medium-grained and composed mainly of hornblende, plagioclase, biotite, pyroxene, apatite, and quartz. Hornblende is brown to green and often encloses minor inclusions of plagioclase and apatite, forming a poikilitic texture (Figure 4a). Plagioclase crystals exhibit zoning with extensive sericitization and epidotization, especially at their cores. Biotite occurs either as isolated crystals or in aggregates and clusters forming a biotite nest fabric. Pyroxene occurs as coarse-grained euhedral prismatic crystals. Quartz crystals occupy the interstitial spaces between the euhedral plagioclase and hornblende crystals. Aggregates of apatite are present in appreciable amounts in the form of acicular and rod-like prisms.

The Dokhan volcanics of SGUM are represented by dacite, which is fine-grained with a porphyritic texture. It is essentially composed of plagioclase, biotite, quartz, and horneblende phenocrysts. Plagioclase occurs as twinned and zoned crystals or aggregates in clusters to form the glomeroporphyritic texture (Figure 4d). Quartz crystals occur in two generations: one constitutes some of the phenocryst and the second occurs as small crystals in the groundmass. Biotite and hornblende occur as euhedral to subhedral long prismatic and six-sided crystals (Figure 4e). Alteration of biotite to chlorite is very common, leaving behind fine magnetite crystals arranged along the cleavage planes.

The granite of SGUM is represented mainly by syenogranite and monzogranite. They are medium-to coarse-grained, equigranular with pronounced myrmekitic and graphic textures (Figure 4b). They consist of plagioclase, quartz, potash feldspar, biotite, and hornblende. Most plagioclase crystals are sericitized, kaolinitized, and epidotized while some of them exhibit an oscillatory zoning. Potash feldspars occur in small amounts as subhedral to anhedral prismatic crystals that are altered to clay minerals. Quartz is found as subhedral to anhedral crystals filling the interstices between the other constituents. Biotite is strongly muscovitized (Figure 4c) along cleavage planes, occurring in the form of euhedral, tabular to prismatic crystals. Hornblende occurs as tabular to prismatic and six-sided crystals that contain small crystals of quartz and plagioclase as inclusions showing a poikilitic texture. Hornblende is altered to both epidote and chlorite.

Microscopically, the diorite of GKZ is medium- to coarse-grained with a hypidomorphic fabric. It is predominantly made up of plagioclase, hornblende, pyroxene, biotite, and quartz. Plagioclase crystals are moderately sericitized with the sericite flakes oriented parallel to the mineral twinning. Hornblende is very common and occurs as mainly pleochroic, medium- to coarse-grained crystals. Some twinned crystals of hornblende are also observed. Pyroxene crystals are mainly subhedral to euhedral with prismatic form. Apatite is abundant and occurs as prismatic to rod-shaped crystals.

The GKZ granodiorite is composed mainly of plagioclase, quartz, biotite with minor amounts of potash feldspar, and muscovite. Plagioclase crystals are highly sericitized with the sericite flakes oriented in one or two directions, one of these directions is parallel to the twinning lamellae. The potash feldspars are represented by sub-prismatic orthoclase and perthite. Quartz-feldspar porphyry is the least abundant rock. The rock is fine grained and composed mainly of plagioclase and quartz phenocrysts with some potash feldspar, hornblende, biotite, pyroxene, and muscovite K-feldspars are mainly represented by subhedral to anhedral prismatic orthoclase and perthite. Hornblende occurs as prismatic crystals forming a corona like texture with pyroxene (Figure 4f). Biotite altered partially or completely to chlorite.

Opaque minerals of the different rock units of SGUM and GKZ are represented by different types of ilmenite-magnetite intergrowth with some discrete grains of homogenous

magnetite and ilmenite. Magnetite is partially altered to martite on cleavage, cracks, and peripheries. Sometimes, it contains fine chalcopyrite crystals as inclusions (Figure 5a). The recorded types of ilmenite-magnetite intergrowth are sandwich (Figure 5b), composite (Figure 5c), banded, fine-network (Figure 5d), external granules, and coarse-trellis. Ilmenite shows extensive alteration to rutile and titanite along cracks and cleavage planes (Figure 5e). Quartz-feldspar porphyry is poor in opaque minerals, which is mainly represented by magnetite and specularite. Magnetite occurs either as discrete or aggregates in clusters in the form of equant to prismatic crystals. Specularite is medium-grained, occurring in the form of flaky or fibrous crystals that crosscut each other (Figure 5f). Other specular crystals of hematite radiate from a common center, forming a fan-shape.
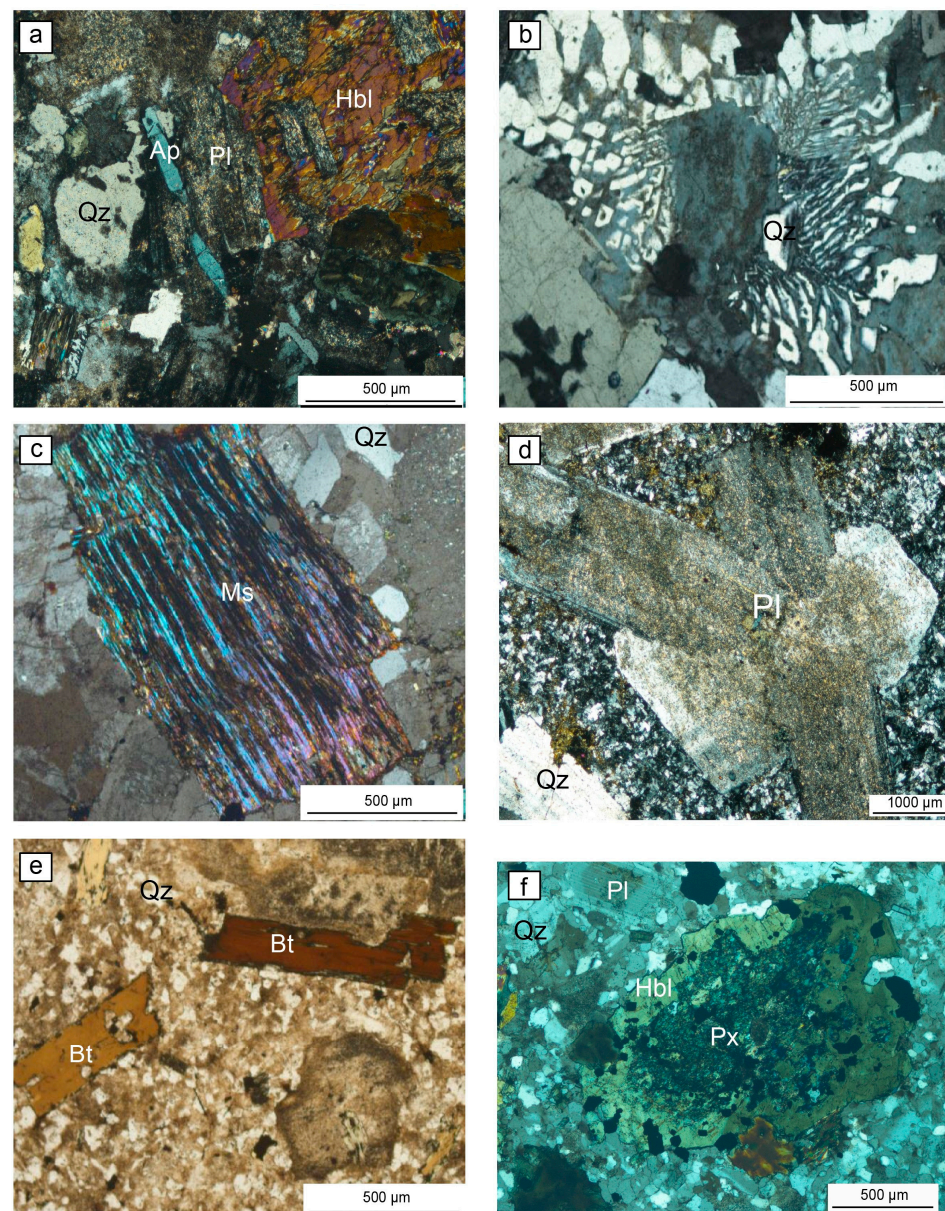

Figure 4. Petrographic features of the country rocks. All photomicrographs (except e) are in Cross-Nicols: (**a**) apatite inclusion in altered plagioclase and a plagioclase inclusion in hornblende forming poikilitic texture in the gabbro of the SGUM; (**b**) myrmekitic and graphic textures in syenogranite of the SGUM; (**c**) highly mucovitized biotite crystal in syenogranite; (**d**) glomeroporphyritic plagioclase crystals in the dacite of the SGUM; (**e**) biotite and quartz phenocrysts in the dacite of the SGUM; (**f**) hornblende forming corona-like texture with pyroxene in the GKZ.
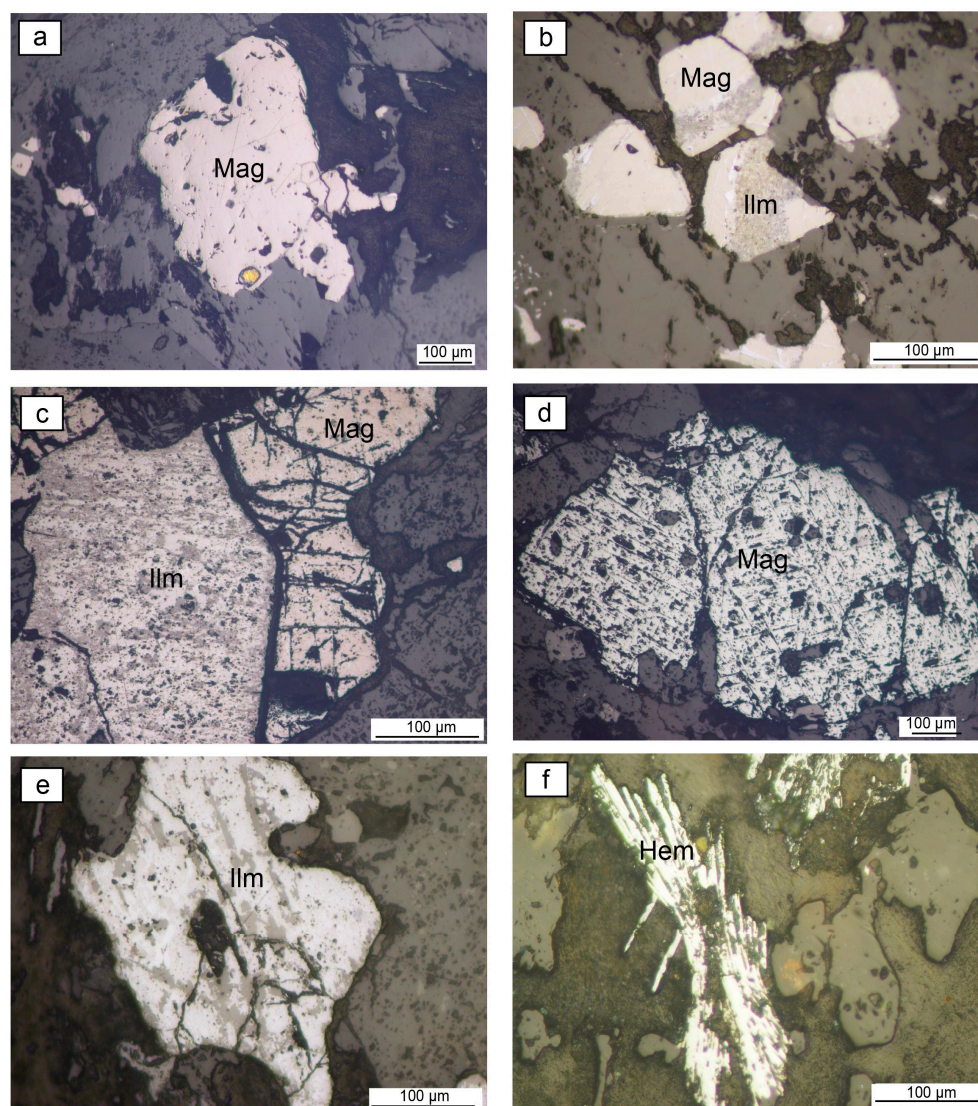
Figure 5. Opaque minerals and their fabrics in the country rocks. All photomicrographs are in reflected light: (**a**) fine chalcopyrite crystal embedded in magnetite in gabbro; (**b**) sandwich-type intergrowth of ilmenite and slight martitized magnetite in gabbro; (**c**) composite grain of magnetite-ilmenite in gabbro. Note the alteration of ilmenite to rutile-hematite and the martitization of magnetite; (**d**) fine trellis of ilmenite-magnetite in syenogranite; (**e**) subhedral ilmenite crystal with patchy alteration to rutile-hematite in the dacite of the SGUM; (**f**) specular hematite crystal in quartz-feldspar porphyry.

5. Ore Paragenesis and Possible Paragenetic Sequence

On the basis of microfabric relations, observations, and styles of deformation, two main events have been distinguished, namely, pre-shearing and post-shearing. The localized effects of shearing are evident through the presence of megascopic and microscopic fractures that lately filled with barite, iron oxides, and sulfides. Iron oxides are represented by specurlarite, magmetite, and geothite whereas pyrite and chalcopyrite are the main sulfide minerals encountered.

Barite occurs as euhderal to subhedral prismatic crystals with high relief and perfect or imperfect two-perpendicular sets of cleavage (Figure 6a). Veinlets of barite were also observed in the alteration zones and quartz veins (SII 3). Sericite is also observed and occurs as coarse-gained crystals filling microfractures together with specularite (Figure 6b). Sericite is also stretched and sheared in the direction of shearing.
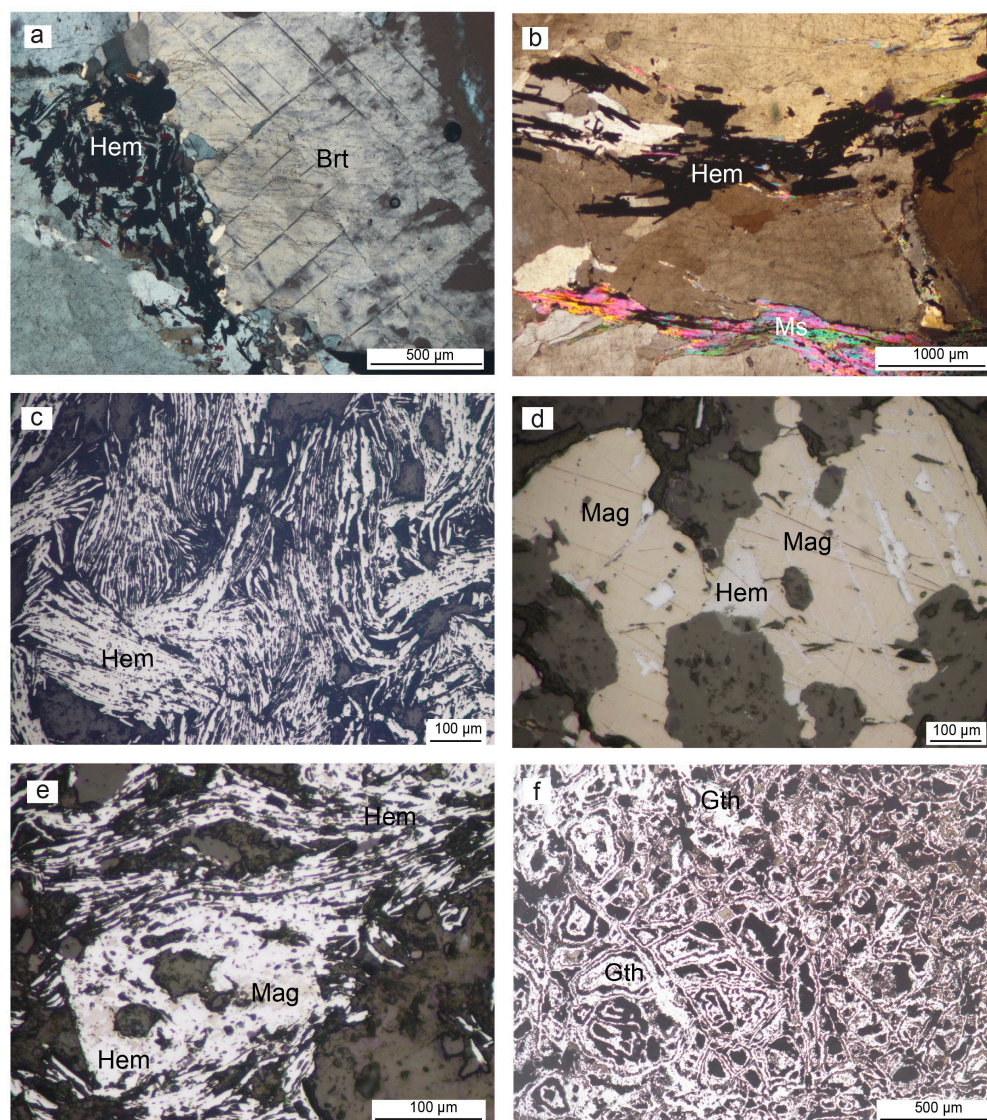
Figure 6. Ore minerals in alteration zones: (**a**) specularite crystals associated with a coarse grained barite crystal that has two perpendicular set of cleavages; (**b**) specularite and sericite crystals filling the pre-existing fractures; (**c**) sheared and crumbled specularite; (**d**) slight martitization in magnetite; (**e**) relics of magnetite in sheared specularite; (**f**) well-developed colloform goethite completely pseudomorphing the magnetite.

Hematite is the most abundant iron mineral in the SGUM and GKZ areas. It usually has a specular or micaceous habit, which is referred to as specularite. The specular hematite is present as flaky crystals that aggregate in bundles that cross cut each other. Two generations of specularite were observed: the first generation was coarse whereas the second generation was fine (microspecularite). It is believed that the first generation formed after the effect of shearing on the pre-existing magnetite whereas the second phase formed synchronously with the second phase of quartz, as proven by the zonal arrangement of microspecularite along the peripheries of the idiomorphic quartz. The formation of specularite follows the formation of magnetite whereas the former is formed due to shearing of the latter. The effect of shearing appears in specularite crystals where most of the grains are stretched as elongated patches or brecciated and cracked. Additionally, some of the specularite crystals are folded and crumbled in an irregular manner (Figure 6c).

Magnetite occurs in different generations and sizes, among them, the coarse-grained crystals are the most common. The pre-shearing generation is partially transformed to spec-

ular hematite where some relics of magnetite are still preserved in specularite (Figure 6e). The post-shearing magnetite is idiomorphic to sub-idiomorphic crystals in the form of equant, prismatic, and six-sided. Martitization is very abundant in the different generations of magnetite, ranging from incipient alteration to martite (normal martitization), to extensive replacement by martite, leaving relics of magnetite within martite (heat martitization) (Figure 6d). Colloform geothite is the main alteration product of either sulfide minerals (oxidized pyrite or chalcopyrite) or oxide minerals in the hydrothermal alteration zones of both the SGUM and GKZ prospects. Spongy-like goethite was observed in some alteration zones at the GKZ prospect (Figure 6f).

Pyrite is the dominant sulfide mineral in the alteration zones and quartz veins. It occurs in different forms and sizes related to two different generations, namely, fresh and oxidized pyrite. It occurs as patches and idiomorphic cubes of different sizes. It is commonly aligned in a planar structure whereas others show random orientations. Oxidized pyrite occurs as individual crystals or as clusters with well-developed crystal faces. It shows intensive oxidation to goethite, while a colloform texture is exhibited (Figure 7b,c).

Chalcopyrite occurs either as anhedral crystals filling microfractures or as fine disseminated crystals in quartz (Figure 7a). Chalcopyrite shows either a slight alteration to goethite (Figure 7d), particularly along fractures and peripheries, or a complete replacement to a well-developed colloform goethite. Sometimes, it partially altered to copper sulfide minerals such as covellite along the fractures and peripheries. The formation of sulfides (pyrite and chalcopyrite) post-dates the formation of iron oxides.
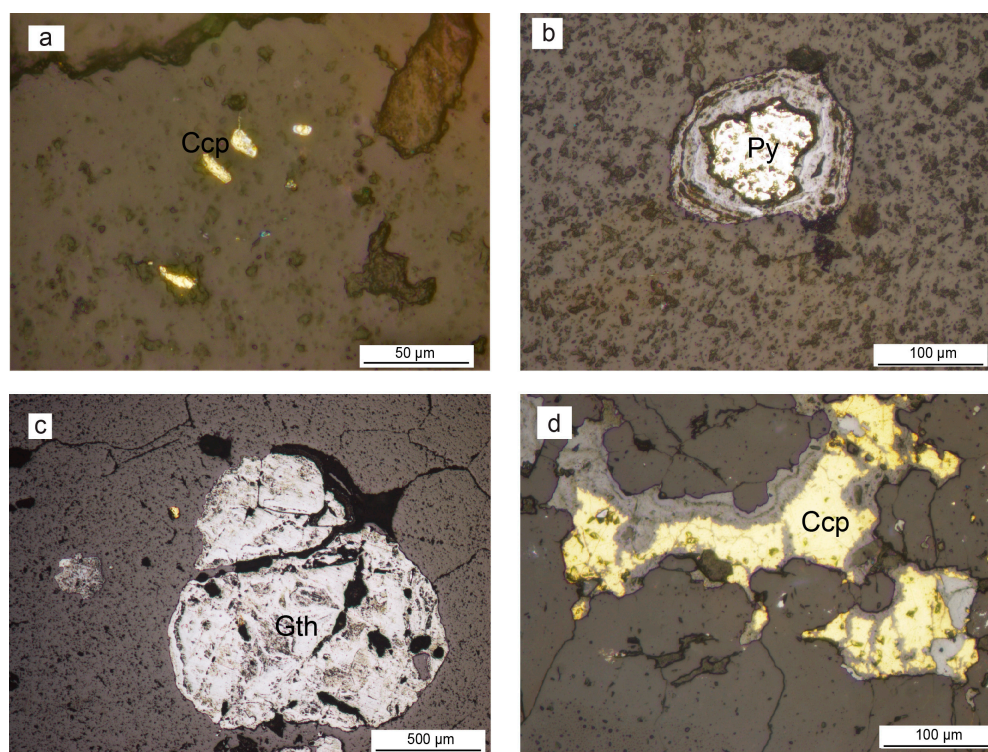

Figure 7. Ore minerals in alteration zones and quartz veins; (**a**) fine fresh chalcopyrite crystals in alteration zones of the SGUM prospect; (**b**) slightly oxidized pyrite in quartz veins in the SGUM prospect; (**c**) goethite crystal formed after the complete oxidation of pyrite in the alteration zones of the SGUM prospect; (**d**) slightly altered chalcopyrite crystal along the peripheries in alteration zones of the GKZ prospect.

Quartz is the dominant gangue mineral in the alteration zones and quartz veins. It occurs in different colors, forms, and sizes related to more than one generation. Smoky, white, and red quartz are observed. The early formed quartz is highly sheared and brecciated.

Idiomorphic grains of quartz (containing fine-grained specularite crystals as inclusions) occurring as islands enclosed in magnetite are very common features. Many xenomorphic quartz crystals contain randomly distributed disseminated pyrite, chalcopyrite, and specularite. Fine gold speaks were observed in two modes in the alteration zones and quartz veins. The first occurred in the form of fine inclusions in xenomorphic and idiomorphic quartz. The second mode was present as free dispersed gold in microfractures (SII 4).

6. Mineral Chemistry

The identification and nomenclature of the essential minerals (feldspar, apatite, dark mica, pyroxene, chlorite, amphibole and Fe-Ti oxides) of the country rocks at the SGUM and GKZ prospects were analyzed using electron microprobe analyses (EPMA) whereas the mineral chemistry of ore minerals within the alteration zones were examined using the energy dispersive X-ray (EDX) technique. The EMPA and SEM-EDX analyses are given in the Supplementary Files SI 1–10 and SII 1–4. The detailed SEM-EDX investigations allow us to define the microfabrics of the primary and secondary ore minerals hosted within the shear zones at the SGUM and GKZ prospects. EDX spectral analyses of the alteration zones show the predominance of oxide and sulfide minerals in addition to barite.

6.1. Feldspars

The EMPA data of both k-feldspar and plagioclase of diorite, Dokhan volcanics, and quartz-feldspar porphyries are listed in the Supplementary Files SI 1 and 2. According to the Or–Ab–An classification diagram (Figure 8a), feldspars of the quartz feldspar-porphyry range from orthoclase to albite-oligoclase and anorthite, while the feldspars in diorite and Dokhan volcanics are orthoclase and anorthoclase. Pure albite crystals were also observed in some crystals of the Dokhan volcanics. The average composition of K-feldspar was $Ab_{12.27}An_{0.42}Or_{87.30}$, $Ab_{26.51}An_{1.10}Or_{72.37}$, and $Ab_{15.20}An_{0.41}Or_{84.83}$ in the samples of diorite, Dokhan volcanics, and quartz-feldspar porphyry, respectively. The average composition of plagioclase was $Ab_{64.94}An_{0.03}Or_{27.45}$, $Ab_{95.32}An_{3.78}Or_{0.88}$, and $Ab_{66.16}An_{30.52}Or_{3.31}$ in the sample of diorite, Dokhan volcanics, and quartz-feldspar porphyry, respectively.

6.2. Apatite

Apatite from the diorite of the GKZ prospect was characterized by a high content of Cl ranging from 2.97 to 9.73 wt%, which may be considered as chlorapatite. It has an average CaO ranging from 55.54 to 56.48 wt%, P_2O_5 from 37.98 to 38.35 wt%, and F from 1.11 to 2.21 wt% (Supplementary File SI 3). The apatite crystals show magmatic origins when plotted on the [47] diagram (Figure 8b).

6.3. Phlogopite

The chemical composition and structural formulae of dark micas from the quartz-feldspar porphyry of the GKZ prospect are listed in the supplementary file SI 4. Dark micas have SiO_2 (32.55–37.96 wt%), Al_2O_3 (13.72–15.42 wt%), MgO (12.84–16.41 wt%), FeO^t (13.28–16.73 wt%), and TiO_2 (1.92–4.128 wt%). According to the classification scheme in [48], the dark mica of quartz-feldspar porphyry can be classified as phlogopite (Figure 9a). In the ternary diagram [49], the examined samples fell in the primary field (Figure 9b). On the FeO^t vs. Al_2O_3 plot in [50], all samples fell in the calc-alkaline field (Figure 9c). All phlogopite crystalized at a high temperature, estimated to be above 720 °C according to the crystallization temperature diagram in [51] (Figure 9d).

6.4. Pyroxene

The chemical analyses and structural formulae of pyroxene from diorite of the GKZ prospect are reported in the supplementary file SI 5. The EMPA analyses showed that the analyzed pyroxene crystals had SiO_2 ranges from 52.84 to 54.12 wt%, MgO ranges from 23.91 to 24.59 wt%, FeO^t ranges from 18.75 to 22.24 wt%, and CaO ranges from 1.79 to

2.74 wt%. According to the ternary diagram [52], this pyroxene can be classified as enstatite (Figure 10a).

6.5. Chlorite

Chlorite is the main secondary mineral encountered in the country rocks at both the SGUM and GKZ prospects. It formed after the partial or complete replacement of biotite and hornblende. Oxide analyses and structural formulae of chlorite from diorite, Dokhan volcanics, and alteration zones are given in the supplementary file SI 6. The Si vs. Fe plot in [53] classifies the chlorite samples of diorite, Dokhan volcanics, and alteration zones as pycnochlorite, diabanite, and ripidolite, respectively (Figure 10b).

6.6. Amphibole

The compositions and structural formulae of amphiboles from diorite and quartz-feldspar porphyry of the GKZ prospect are reported in SI 7. According to the classification scheme in [54], amphiboles in diorites range in composition from Ca-rich amphiboles to Mg-Fe-Mn rich amphiboles. The latter is represented by anthophyllite whereas the former is represented by tremolite (Figure 10c). The studied tremolite generally contains varying SiO_2 (53.30–56.28 wt%), MgO (16.57–20.73 wt%), and FeO^t (7.64–9.82 wt%) compositions. Anthophyllite is enriched in FeO^t (12.69–15.34 wt%) compared to tremolite. All of the amphibole crystals in quartz-feldspar porphyry are calcic, ranging from actinolite to hornblende (Figure 10d). The low Al_2O_3 and FeO^t contents of amphiboles support their magmatic nature [55].
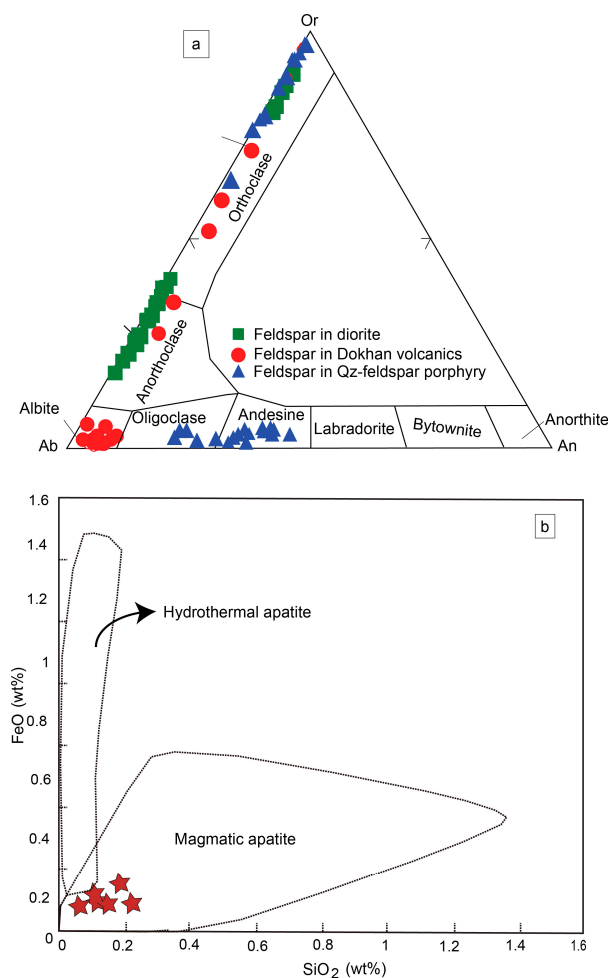

Figure 8. (**a**) Plots of feldspar composition using the Or–Ab–An diagram [56]; (**b**) distinction between magmatic and hydrothermal apatite in diorite of the GKZ prospect [47].
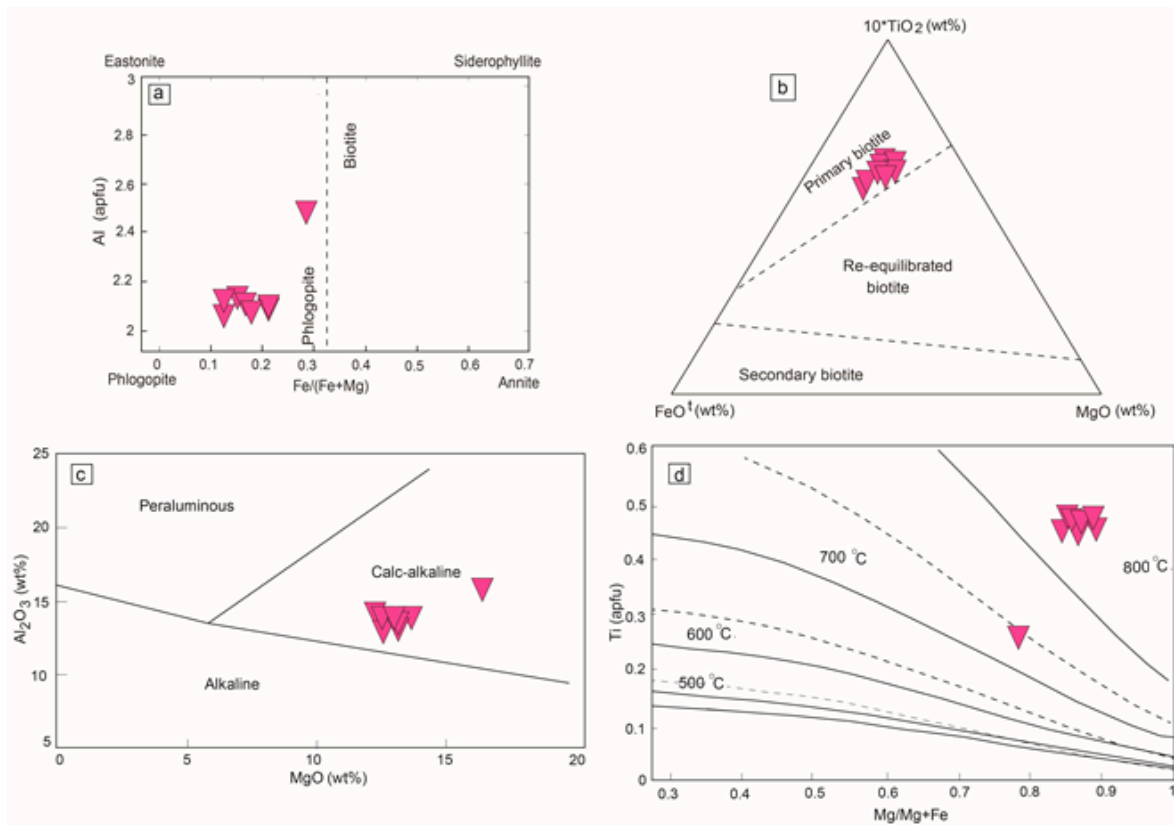
Figure 9. (**a**) Composition of dark mica using $Fe^{2+}/(Mg + Fe^{2+})$ vs. Al diagram [48]; (**b**) MgO–FeO^t-TiO$_2$*10 ternary diagram [49]; (**c**) FeO^t vs. Al$_2$O$_3$ discrimination diagram for the analyzed mica [50]; (**d**) crystallization temperature of the analyzed mica [51].

Figure 10. (**a**) Quadrilateral classification diagram of pyroxene in diorite [52]; (**b**) composition of the analyzed chlorite using the diagram in [53]; (**c**,**d**) classification of the analyzed amphiboles using diagrams in [54].

6.7. Fe-Ti Oxides

Fe-Ti oxides are the most common opaque minerals in the country rocks and are represented mainly by magnetite and ilmenite. The major elements and structural formulas of Fe-Ti oxides are reported in the supple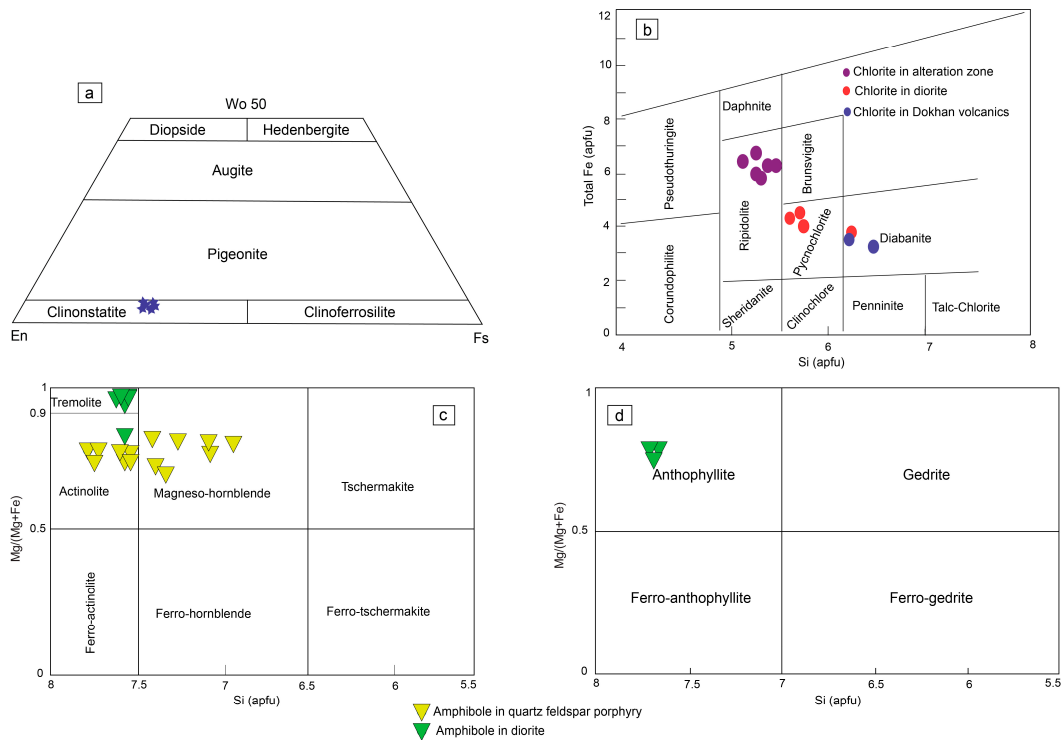mentary files SI 8 and 9. According to the EMPA data, the studied magnetite has FeO^t varying from 95.38 to 97.55 wt%, 79.09 to 81.11 wt%, and 77.56 to 81.37 wt% for diorite, Dokhan volcanics, and quartz-feldspar porphyry, respectively, with negligible amounts of the other oxides (supplementary file SI 8). On the other hand, ilmenite was analyzed only in diorite and it occurred either as homogenous discrete crystals or intergrown with magnetite. The analyzed ilmenite had TiO_2 ranges from 40.61 to 46.43 wt% and FeO^t ranges from 48.71 to 53.35 wt% (supplementary file SI 9).

7. Whole-Rock Geochemistry

The results of the whole analyses of the volcanic and plutonic rocks from the SGUM and GKZ area are listed in Tables 1 and 2. The dacite of GKZ was characterized by a high SiO_2 content (68.57–69.03 wt%) compared to the volcanic rocks of SGUM (60.24–67.49 wt%). Dacite of the SGUM and GKZ areas showed a narrow variation in major oxides and both were characterized by a high alkali content (Na_2O = 0.79–5.32 wt% and K_2O = 2.58–5.17 wt%) and Al_2O_3 (13.18–15.54 wt% at SGUM and 12.22–14.76 wt% at GKZ). The CaO content (0.98–4.06 wt%) at SGUM predominated over that (0.41–2.36 wt%) in the GKZ area. The TiO_2 and P_2O_5 contents were very low, and the MgO contents in the SGUM and GKZ areas ranged from 1.14 to 4.04 wt% and 0.96 to 1.92 wt%, respectively.

The geochemical data of the studied syenogranite and monzogranite showed some enrichment in the SiO_2 content (ranges from 63.07 to 66.6 wt%). The K_2O (3.71–6.26 wt%) and Na_2O (2.61–4.27 wt%) contents in syenogranite were high due to the modal percentage of feldspars (Table 2). It was noticed that the average composition of major oxides of granodiorite in the GKZ were comparable with the syenogranite and monzogranite in the SGUM area but the granodiorite had a slight depletion in CaO, Na_2O, and TiO_2. The average CaO in granodiorite was 0.37 wt%, which was low due to small amounts of mafic minerals. The younger gabbro of the SGUM prospect is characterized by a remarkably high SiO_2 content (average of 56.26 wt%). The analyzed samples of diorite in the GKZ area showed a wide range of SiO_2 (51.34 to 57.79 wt%). Gabbro and diorite showed remarkable contents of iron oxide with an average of 8.06 and 8.22 wt%, respectively. These values are high due to the high percentage of ferromagnesian minerals (biotite, hornblende, and pyroxene) in these rocks. In general, the studied rocks in both the SGUM and GKZ areas showed a remarkably high content of Ba (510–41,765 ppm), Cu (45–20,499 ppm),and Sr (153–1474 ppm) (Tables 1 and 2). Based on the variation diagram of major elements, all rock varieties had high concentrations of Al_2O_3 and Na_2O.

Volcanic rocks of the SGUM and GKZ areas were geochemically classified using the diagrams in [57,58]. The results of plotting of the analytical data using these diagrams were in harmony with the microscopic identification. Quartz-feldspar porphyry in GKZ lay in dacite and rhyolite fields of (Na_2O + K_2O) versus the SiO_2 diagram by [57] whereas the Dokhan volcanics of SGUM fell in the fields of trachyandesite, dacite, and rhyolite (Figure 11a). According to the Zr/TiO_2 against Nb/Y classification diagram of volcanic rocks, the analyzed samples mainly fell in the field of rhyodacite (Figure 11b). The nomenclature and chemical classification of the investigated plutonic rock were determined using the alkali silica discrimination diagrams or the so-called TAS diagram by [59] (Figure 11c). The studied gabbro of the SGUM area was plotted in the monzodiorite and diorite field. In this diagram, diorite from the GKZ area fell within the fields of monzogabbro, monzodiorite, and monzonite. Granitic rocks of the SGUM area fell in the field of the quartz monzonite diagram whereas the granitoids in the GKZ plot were in the monzonite field.

Table 1. Major oxides (wt%) and trace element (ppm) data of the studied volcanics at the SGUM and GKZ prospects.

	South Gabal Um Monqul					Gabal Al Kharaza		
	Dacite					Quartz-Feldspar Porphyry		
Sample No.	Ma8	Ma11	Ma12	Ma13	Ma16	Da1	Da5	Da6
Major oxides (wt%)								
SiO_2	65.77	63.18	60.24	67.49	62.91	68.57	67.22	69.03
TiO_2	0.38	0.45	0.63	0.49	0.59	0.45	0.47	0.42
Al_2O_3	13.18	14.76	15.83	15.34	15.54	14.36	14.76	12.22
Fe_2O_3	4.47	5.46	6.59	4.62	7.24	3.84	4.03	7.41
MgO	1.14	2.97	4.04	1.73	1.59	1.67	1.92	0.96
CaO	1.12	2.26	4.06	0.98	1.56	0.86	2.36	0.41
Na_2O	3.39	3.67	4.34	4.59	5.32	3.38	3.77	0.79
K_2O	5.17	3.96	2.58	3.11	2.85	4.23	3.84	4.32
P_2O_5	0.16	0.16	0.19	0.16	0.17	0.12	0.12	0.09
MnO	0.27	0.18	0.08	0.24	0.06	0.03	0.13	0.01
LOI	1.31	1.92	1.44	1.31	1.28	1.82	1.25	3.83
Total	96.36	98.97	100.02	100.06	99.11	99.33	99.87	99.49
Trace elements (ppm)								
Rb	102.57	82.62	70.08	82.13	82.57	50.21	133.41	152.47
Ba	23,990.55	1294.3	631.17	969.67	738.76	719.62	1468.02	759.23
Sr	945.74	366.5	574.27	232.47	251.72	742.61	385.34	258.42
Nb	8.98	7.06	6.31	12.42	12.03	6.16	9.81	12.63
Zr	235.31	165.61	163.65	186.88	199.53	192.5	183.97	163.48
Hf	7.43	4.42	3.28	6.15	4.35	3.89	3.9	15.77
Y	26.17	16.63	17.19	38.91	42.26	21.83	19.14	10.01
Zn	27.41	20.68	29.32	15.99	28.54	51.01	28.25	235.58
Cu	99.89	221.29	45.45	454.17	107.57	57.4	235.74	2497.81
Ni	8.51	64.12	147.8	<d.l.	140.81	35.44	37.94	42.95
Co	6.14	14.78	23.83	6.33	9.45	23.98	13.01	12.12
Cr	<d.l.	191.43	289.81	<d.l.	222.29	70.92	75.28	92.35
V	143.35	78.46	114.48	27.19	33.82	162.92	69.21	71.73
Pb	20.02	14.65	22.64	17.07	22.27	24.53	25.02	49.38
Th	3.54	5.85	3.67	4.23	7.59	<d.l.	13.45	7.05
Ta	0.02	0.02	0.02	0.02	0.03	0.06	0.04	0.04
U	0.21	0.29	0.11	0.14	0.15	0.43	0.34	0.59
Mo	0.38	0.56	0.57	0.07	1.69	0.53	0.13	3.48
Cs	<d.l.	0.01	0.01	0.11	0.03	0.08	0.14	0.17
Rare-earth elements (ppm)								
La	2.32	0.90	1.04	1.83	2.15	1.32	1.16	1.11
Ce	3.94	1.98	2.10	3.67	4.20	2.41	2.27	1.92
Pr	0.44	0.19	0.26	0.43	0.505	0.275	0.25	0.21
Nd	1.66	0.78	1.07	1.73	2.005	1.01	0.90	0.67
Sm	0.39	0.12	0.18	0.36	0.38	0.21	0.18	0.14
Eu	0.08	0.03	0.04	0.08	0.08	0.04	0.03	0.02
Gd	0.24	0.10	0.15	0.30	0.36	0.18	0.13	0.11
Tb	0.03	0.01	0.02	0.04	0.05	0.02	0.02	0.01
Dy	0.20	0.08	0.12	0.30	0.37	0.17	0.12	0.10
Ho	0.04	0.01	0.02	0.06	0.07	0.03	0.02	0.02
Er	0.11	0.04	0.06	0.19	0.22	0.08	0.06	0.05
Tm	0.01	0.007	0.009	0.03	0.03	0.01	0.009	0.008
Yb	0.11	0.04	0.05	0.20	0.23	0.07	0.05	0.04
Lu	0.01	0.008	0.01	0.03	0.03	0.011	0.008	0.007

Table 2. Major Oxides (wt%) and trace element (ppm) data of the plutonic rocks from the SGUM and GKZ prospects.

|	South Gabal Um Monqul					Gabal Al Kharaza							
	Monzo-to Syenogranite					Gabbro		Granodiorite			Diorite		
Sample No.	Ma3	Ma4	U1	U3	U13	Ma17	Ma18	Db1	Db5	Dc1	Dc3	Dd1	Dd2
Major oxides (wt%)													
SiO_2	63.07	66.61	66.47	63.42	65.05	54.25	58.27	63.14	60.51	57.79	51.34	53.14	52.27
TiO_2	0.5	0.62	0.58	0.53	0.57	0.94	0.85	0.4	0.33	0.87	1.06	0.92	1.12
Al_2O_3	13.87	16.08	15.18	13.13	14.8	15.71	16.22	13.16	11.96	15.28	15.52	18.71	17.5
Fe_2O_3	5.24	5.86	3.92	7.11	4.25	8.57	7.56	5.97	9.99	6.66	8.57	7.81	9.84
MgO	1.14	0.78	1.31	0.67	1.34	5.44	4.02	1.62	1.42	5.36	3.29	4.34	4.52
CaO	1.11	0.19	2.16	2.54	0.51	5.84	5.31	0.36	0.39	4.81	7.17	7.66	3.16
Na_2O	3.47	<d.l.	4.27	2.61	3.78	3.87	4.01	1.92	2.64	3.94	3.76	3.83	5.08
K_2O	4.55	5.56	3.71	6.26	4.14	2.22	1.89	5.19	4.06	2.53	1.26	1.42	1.92
P_2O_5	0.17	0.16	0.18	0.17	0.15	0.24	0.22	0.13	0.13	0.25	0.32	0.32	0.41
MnO	0.12	0.12	0.08	0.14	0.06	0.17	0.19	0.15	0.03	0.13	0.21	0.16	0.16
LOI	1.47	2.71	1.26	2.85	2.76	1.99	1.51	2.07	1.81	1.54	7.38	1.35	3.61
Total	94.71	98.68	99.12	99.43	97.41	99.24	100.05	94.11	93.27	99.16	99.88	99.66	99.59
Trace elements (ppm)													
Rb	96.14	138.27	93.28	130.97	97.39	52.88	49.23	198.82	158.89	70.3	39.45	40.56	90.65
Ba	32,594.07	3249.91	1094.4	2238.32	1981.13	642.75	705.51	29,092.97	41,765.85	682.16	3055.32	510.45	2505.07
Sr	1373.01	181.31	639.17	213.23	483.74	653.01	728.05	1026.01	1474.68	536.04	701.08	789.42	470.97
Nb	7.36	12.42	10.56	9.85	9.80	6.97	6.04	10.73	11.97	7.37	5.28	2.89	6.17
Zr	268.54	197.98	245.77	175.19	214.56	162.37	188.73	225.54	249.39	182.45	150.84	125.49	105.38
Hf	7.79	9.26	8.25	5.47	92.77	4.92	3.82	46.49	18.88	4.94	3.44	3.22	19.33
Y	13.95	11.86	12.81	14.24	13.94	17.73	21.41	19.15	15.95	20.01	18.61	16.13	18.23
Zn	27.21	19.13	53.32	24.38	76.68	43.17	50.01	19.52	26.06	44.94	114.46	56.28	60.75
Cu	101.64	1097.61	453.18	313.86	17494.88	55.73	56.28	8258.4	2099.78	104.03	91.26	110.05	3293.18
Ni	8.14	8.15	50.94	5.15	47.38	96.23	34.75	59.36	165.99	109.69	136.17	138.54	122.06
Co	4.83	4.32	14.41	10.46	47.52	31.23	23.51	40.98	8.07	17.93	34.13	27.46	35.34
Cr	<d.l.	3.92	68.94	6.98	57.75	253.22	69.51	37.97	181.34	241.22	303.52	204.74	96.22
V	209.91	99.66	60.29	69.19	66.92	167.92	159.73	195.61	279.54	132.69	194.93	169.48	209.79
Pb	23.11	14.59	23.12	25.12	20.86	15.51	24.05	12.09	15.71	18.73	18.07	17.16	19.01
Th	7.96	11.31	10.46	9.19	10.26	<d.l.	<d.l.	15.23	11.87	<d.l.	<d.l.	<d.l.	2.18
Ta	0.03	0.03	0.03	0.02	0.04	0.02	0.01	0.07	0.05	0.01	0.01	0.01	0.01
U	0.18	0.47	0.25	0.15	0.63	0.08	0.06	0.29	0.46	0.04	0.04	0.04	0.34
Mo	0.34	2.53	0.43	0.07	0.46	0.04	<d.l.	0.17	2.72	<d.l.	0.01	0.48	2.64
Cs	0.05	0.09	0.06	0.08	0.05	0.02	0.04	0.08	0.06	0.08	0.11	0.06	0.05
Rare-earth elements (ppm)													
La	2.49	2.17	1.87	2.36	1.27	1.02	0.89	1.01	5.89	0.73	1.15	0.84	1.02
Ce	4.13	3.61	3.41	4.50	2.66	2.09	1.86	2.13	8.97	1.50	2.39	1.77	2.18
Pr	0.40	0.38	0.36	0.50	0.29	0.25	0.23	0.23	0.84	0.19	0.29	0.21	0.26
Nd	1.43	1.22	1.32	1.83	1.09	1.04	0.90	0.91	2.68	0.77	1.19	0.85	1.03
Sm	0.19	0.18	0.23	0.32	0.23	0.22	0.20	0.16	0.40	0.17	0.24	0.19	0.22
Eu	0.08	0.06	0.05	0.10	0.06	0.06	0.05	0.04	0.20	0.04	0.06	0.06	0.07
Gd	0.16	0.12	0.16	0.25	0.18	0.16	0.19	0.12	0.30	0.18	0.24	0.16	0.20
Tb	0.02	0.01	0.02	0.03	0.02	0.02	0.03	0.01	0.02	0.03	0.03	0.02	0.02
Dy	0.09	0.07	0.13	0.12	0.14	0.14	0.18	0.10	0.13	0.174	0.21	0.12	0.15
Ho	0.01	0.01	0.02	0.02	0.02	0.02	0.03	0.02	0.02	0.034	0.04	0.02	0.03
Er	0.05	0.04	0.07	0.04	0.07	0.07	0.09	0.05	0.05	0.09	0.10	0.06	0.08
Tm	0.08	0.05	0.01	0.06	0.01	0.01	0.01	0.09	0.08	0.01	0.01	0.09	0.01
Yb	0.05	0.03	0.06	0.03	0.08	0.07	0.08	0.06	0.05	0.08	0.09	0.05	0.07
Lu	0.08	0.05	0.09	0.06	0.01	0.01	0.01	0.01	0.08	0.01	0.01	0.08	0.01
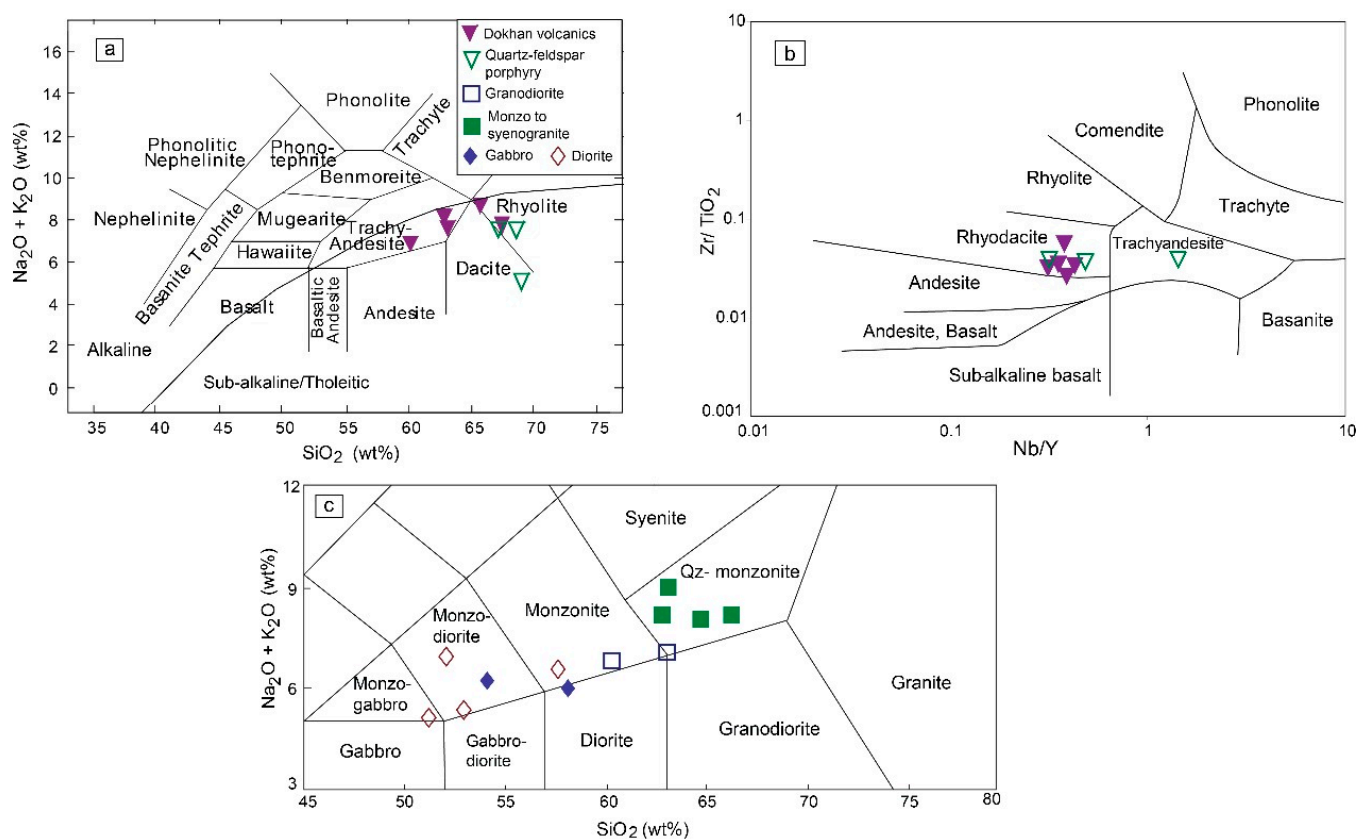
Figure 11. Geochemical classification diagrams of the country rocks in the SGUM and GKZ prospects: (**a**) total alkali oxide silica diagram in [57]. The dividing line was taken from [60]; (**b**) Zr/TiO_2 vs. Nb/Y diagrams in [58]; (**c**) TAS diagram in [59]. Symbols are as shown in Figure 11a.

8. Discussion

8.1. Petrogensis of the Host Rocks

8.1.1. Magma Type and Source

The concentrations of major and trace elements fluctuated significantly among the various studied rocks, which clearly suggests that a variety of processes and sources were involved in their production [61]. Using the aluminum saturation index (ASI) in [62], the studied gabbro and diorite showed a metaluminous nature while the dacite and granitic rocks had a transition between the metaluminous and peraluminous natures (Figure 12a). The presence of secondary kaolinite may be responsible for the peraluminous quality of the dacite samples. All of the studied rock units were also enriched in K_2O and belong to the high-K calc-alkaline to shoshomite series in [63] (Figure 12b). This is supported by the AFM diagram in [60], where all of the studied rocks plotted in the calc-alkaline field (Figure 12c). The composition of phlogopite confirms the interpretation from the whole-rock geochemistry data. All phlogopite data from the quartz feldspar porphyry plotted completely in the calc-alkaline field in the discrimination diagram in [51] (Figure 9c). Actually, the geochemical characteristics of these rocks are connected to the calc-alkaline subduction rocks that originate from orogenic belts [64].

In continental arc environments, it is anticipated that during its storage at the base of the continental arc crust, crustal melting and assimilation will change the chemistry of the parent mantle-derived magma [65]. The high-K calc-alkaline composition of the dacite in the studied areas would point to a thicker, more developed continental crust that served as the core for the continental arc. The dacitic magma was formed by the melting of hydrated calc-alkaline and high-K calc-alkaline amphibolitic rocks rather than having an underlying thick continental crust based on its high potassic nature [66].
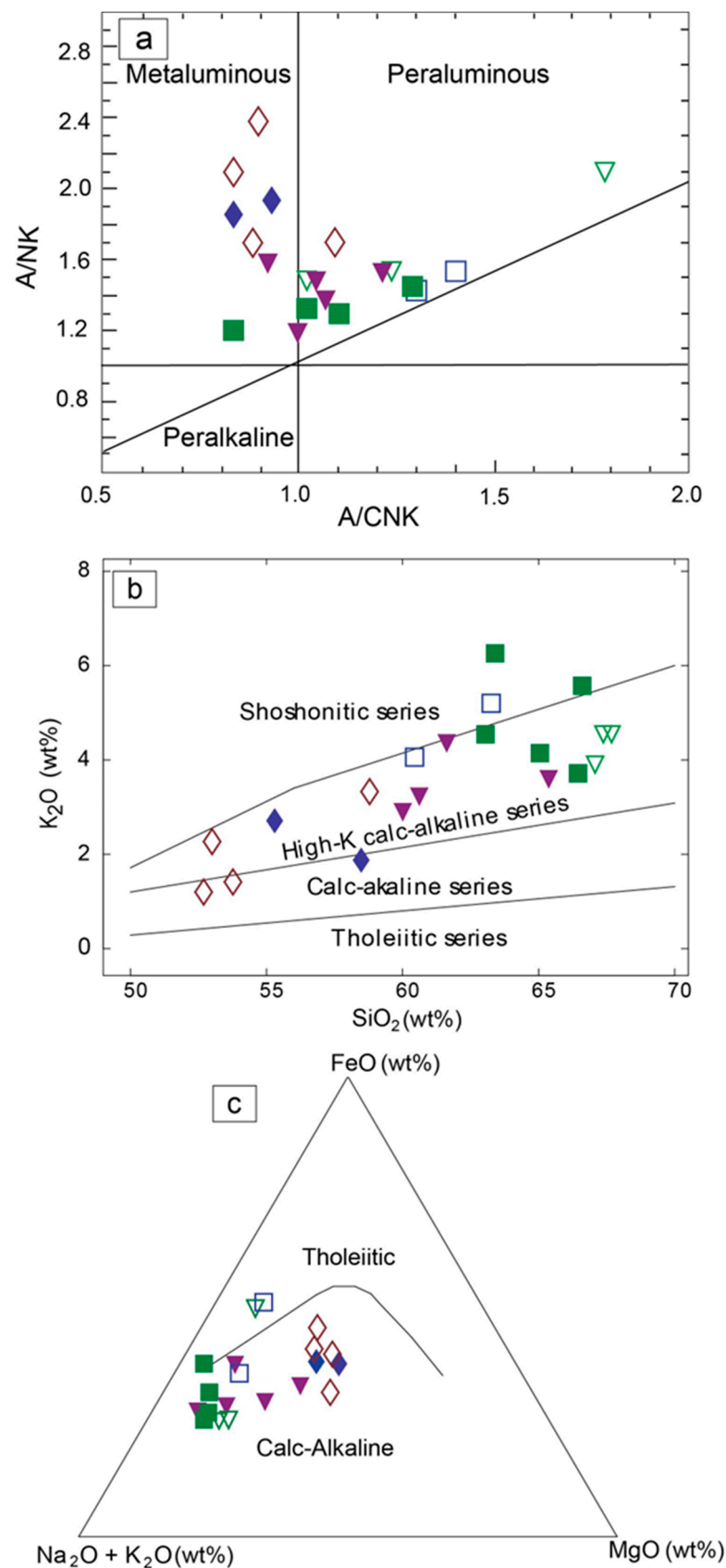
Figure 12. Magma type for the country rocks using the (**a**) diagram in [62]; (**b**) diagram in [63]; (**c**) AFM ternary diagram in [60]. Symbols are as shown in Figure 11a.

Many petrogenetic mechanisms have been proposed for the formation of the studied granites. These granites may be formed by fractional crystallization processes from high K-appinitic magmas [67]. However, the large variation in La/Yb (15.84–109.22) is not consistent with fractional crystallization processes [68]. Another possibility is that these granitic rocks may have been produced from the partial melting of a thickened mafic lower crust [69]. According to [70], granitic melts might have developed from the partial melting of a variety of crustal rocks including amphibolites, pelites, and metagraywackes. The petrographical investigation and whole-rock geochemistry are comparable to the melting of an amphibolitic source. This is supported by the high La/Yb and Sr/Y ratios, which were similar to the geochemical evidence provided by granitic melts generated by melting a metamorphosed basaltic source, as recorded by [71].

Dacite and granites have remarkably comparable geochemical properties. According to [72], the geochemistry of the felsic melts reflects the inherited environment in which the raw materials were generated rather than the tectonic context of creation. Therefore, rather than having originated in a comparable tectonic environment, the similarities between monzogranite and dacite suggest their derivation from a similar lower crustal material.

8.1.2. Tectonic Environment and Geodynamic Implication

It is believed that whole-rock chemistry may be used to determine the tectonic settings under which the magmas formed. The primary debate concerning the Dokhan volcanic rocks are whether or not they originated during a post-orogenic transitional stage between subduction and extension, or if they developed in a subduction zone setting from extension after crustal thickening [73,74]. The studied Dokhan volcanic rocks, represented by dacite along with quartz-feldspar porphyry, had a pronounced depletion in Nb, Ti, and Rb with an enrichment in Th, Ba, and LILE (SIV). These characteristic features are comparable to subduction zone-related tectonic settings [75]. This is supported by the Zr vs. TiO_2 plot [76] in which the volcanic rocks fell in the volcanic arc field (Figure 13a). Based on the Sr/Y versus Y diagram suggested by [77], all of the studied volcanic rocks had high Y and low Sr contents, giving them a normal island arc character (Figure 13b), which is evidenced by the discrimination diagram in [78] (Figure 13c). According to [79], the differentiation between the oceanic and continental volcanic arc can be detected based on Nb/Yb and Th/Yb ratios. The studied volcanic rocks had a high Th/Ta (176.25–336.25) ratio, which suggests a continental arc system.

The studied granodiorites and monzo- to syenogranites were derived from high-K calc-alkaline magmas that formed in both continental arc and post-collisional settings [80]. In the tectonic discrimination diagram in [81], it is clear that the studied granites fell in the fields of post-collisional and volcanic arc granites (Figure 13d). The high Th/Ta ratio of the studied granitic rocks (217–459.5) suggests subduction-related magmatism rather than within-plate settings. According to [42,82], the examined volcanic and plutonic rocks exhibited a high LILE content compared to HFSE, indicating a continental arc context associated with subduction. The increase in Y contents, which further suggests an arc affinity and indicates that the parent magma was generated in an arc setting or partial melting of a rock produced within an arc, supports this arc setting.

The ANS is seen as an anomaly, despite the fact that juvenile components formed in continental arcs are thought to be the primary building blocks in the post-Archean accretionary orogeny [79]. It has been suggested that the oceanic arc tectonic environment is primarily where the juvenile components of the ANS were generated. However, as shown by [83], the geochemical properties of the volcanic rocks confirm the NED's affinity for continental arcs.
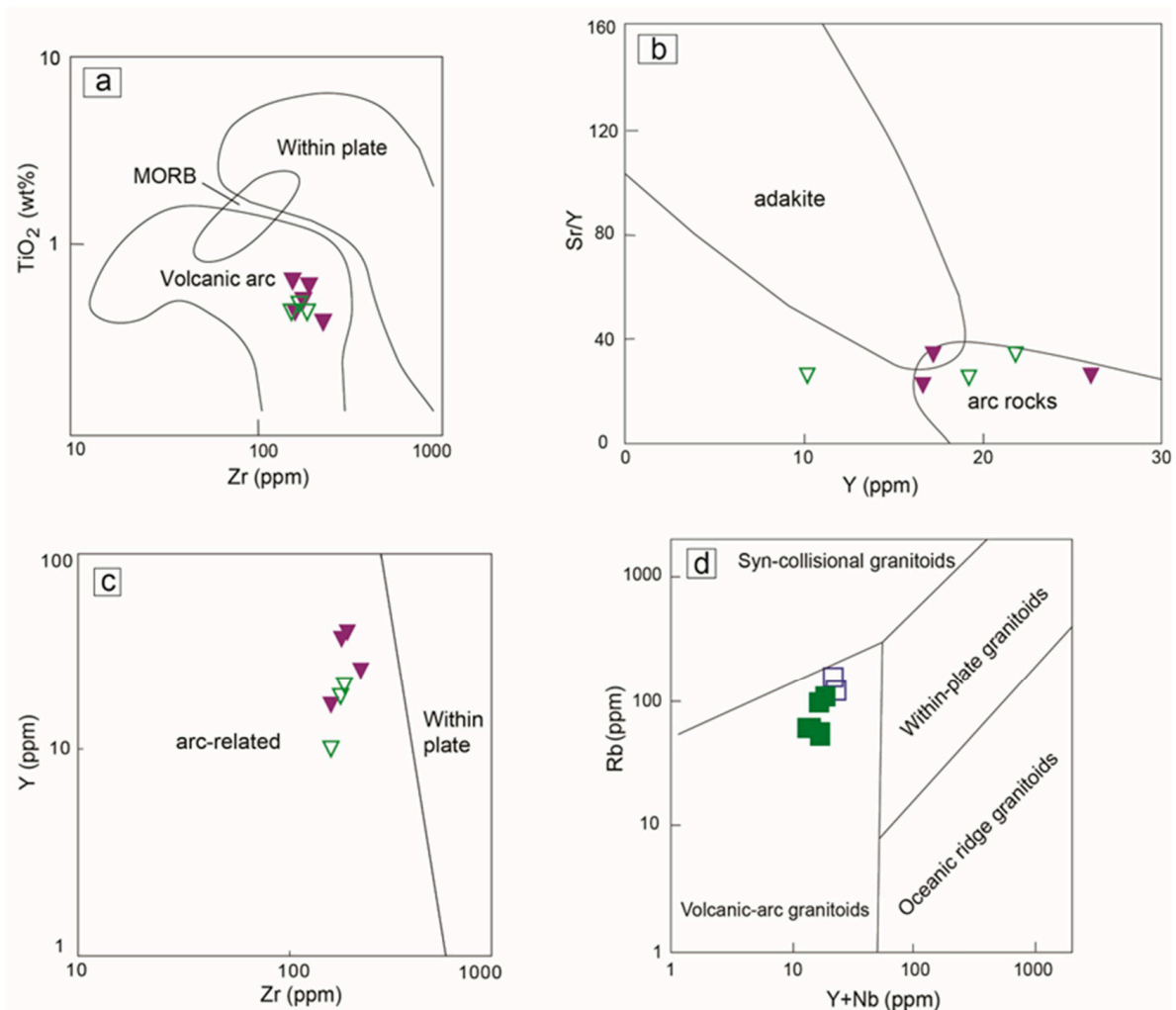
Figure 13. Tectonic setting of the volcanic rocks: (**a**) plot of the Dokhan volcanics in the island arc field in the TiO$_2$ vs. Zr discrimination diagram in [76]; (**b**) Y against Sr/Y diagram in [77]; (**c**) Y vs. Zr discrimination diagram in [78]; (**d**) Rb vs. Y + Nb diagram after [81]. Symbols are as shown in Figure 11a.

8.2. Metallogenesis of Ore Types (Ore Characterization and Ore Genesis)

The gold and copper mineralizations are hosted in structurally controlled shear zones and fractures that lately filled with hydrothermal fluids. The shear zones are mostly aligned in a NW–SE direction at the GKZ prospect whereas a NE–SE direction represents the main trend at the SGUM prospect. On the basis of microscopic investigations, EDX (supplementary file SII 4), and fire assay techniques (supplementary file SI II), the enrichment of gold in both the hydrothermal alteration zones and associated quartz veins at the SGUM and GKZ prospects was revealed. Results from the EDX analyses showed that gold in both alteration zones and the quartz vein samples contained a considerable amount of Ag, amounting to 22.2% and 24.5%, respectively. Such analyses suggest that gold inclusion in quartz and fractures are Ag-rich and can be considered as "electrum" (supplementary file SII 4). The fire assay results of the country rocks were in the range of 0.72 to 1.1 g/t and 0.62 to 0.72 g/t at the SGUM and GKZ prospects, respectively (supplementary file SI II). The assay of alteration zones and quartz vein samples at the GKZ prospect resulted in considerable amounts of gold (0.36 to 3.3 g/t). EMREA [41] detected similar gold contents comparable to the results that we had obtained from the alteration zones and associated quartz veins. In contrast, the alteration zones and quartz veins at the SGUM prospect assayed gold in a much lower range from 0.15 to 0.58 g/t. Osman [40] and Botros and

Wetait [21] recorded gold specks in sulfides and magnetite in the SGUM, respectively. However, a detailed opaque mineralogical study revealed that both sulfides and magnetite were free of any gold peaks within their structures. EDX analyses of some selected samples from the alteration zones showed the enrichment of copper minerals (mainly chalcopyrite) (Supplementary File SII 2). The copper minerals were altered to secondary copper minerals (Supplementary File SII 2). Hydration of Fe-Cu sulfides led to the formation of secondary Cu minerals (copper silicate and copper oxides) in addition to native and electrum gold (Supplementary File SII 2).

Orogenic gold and copper deposits are spatially associated in many magmatic–hydrothermal systems including porphyry copper styles [25–27,84,85] and IOCG deposits [32,36]. Globally, there are two main styles of mineralizations rich in iron oxides: IOCG and iron oxide-apatite (IOA) deposits. IOCG and related deposits are found in three main geological and tectonic settings: (1) the intra-continental orogenic tectonic setting, (2) the post-orogenic or anorogenic tectonic setting, (3) rift of a subduction-related continental margin [30,36,39,86–89]. The IOCG and related deposits are commonly associated with intermediate and acidic igneous rocks [86]. The country rocks that host IOCG deposits are exposed to intense alkali (sodic, potassic and calcic) alteration as albitization, sericitization, silicification, epidotization, and chloritization [30,33,39,90,91]. The main ore associated with IOCG deposits include magnetite, hematite, goethite, pyrrhotite, barite, chalcopyrite, pyrite, bornite, chalcocite, uranium, and gold [27,34,38,39,86]. Magnetite and hematite are the main iron ore in IOCG deposits [27,33,39,40]. Fe-Cu sulfides are not abundant in an IOCG system in comparison to iron oxide minerals [88,92]. In terms of paragenetic sequence, hematite formed at a late stage after magnetite [38]. Chalcopyrite, pyrite, uranium, copper, and gold post-dates the formation of magnetite and hematite [30,39,71]. Three main types of gold deposits are documented in IOCG deposits: (1) native gold [93,94], (2) electrum gold [34,95], and (3) gold–bismuth–antimony–tellurium alloy [96]. Electrum and native gold are the most common types and occur either as inclusions in magnetite, hematite, sulfides, and gangue minerals (quartz, barite and calcite) or as fine particles filling fractures in sulfides and quartz [27,34,97–100].

Genesis of gold and copper mineralization at the SGUM prospect is explained as a porphyry copper system by [21] whereas [40] described the source of gold and copper in terms of iron oxide-rich Cu-Au porphyry-style systems (IOCG). Abd El-Rahman [27] distinguished two main phases for Au-Cu mineralization at the SGUM prospect: the older one (Cu-Mo porphyry-style system), which is related to the Tonain porphyry dacite, whereas the younger system is associated with the Ediacaran post-collisional monzogranite with fingerprints of iron oxide-rich Cu-Au porphyry-style systems rather than IOCG deposits. Our results at the SGUM and GKZ prospects were compared to those from other IOA and IOCG deposits globally, but lacked the typical characteristics observed in IOA deposits, enhancing the potential that they may be a component of IOCG deposits. On the basis of the geochemical characteristics of the host rocks (Figure 13), the subduction-related continental margin is the most suitable setting for IOCG deposits at the SGUM and GKZ prospects. The hydrothermal deposits at SGUM and GKZ show similarities in geological and tectonic setting, alteration products of the host rocks, ore mineral assemblages, paragenetic sequence, and mode of occurrence of gold deposits. However, they have a deficiency in extensive sodic alteration, absence of uranium, and an enrichment in sulfides and barite, which are considered to be the main differences from the IOCG deposits. Thus, the authors suggest that the style of Au-Cu mineralization at the SGUM and GKZ prospects is not that of a typical IOCG, but might be a part of an IOCG deposit. The detailed field and microscopic investigations revealed that the Ediacaran phase of the hydrothermal IOCG deposits is the most dominant phase at the GKZ prospect. The IOCG deposits are hosted in monzogranite and syenogranite at the SGUM prospect whereas diorite, quartz-feldspar porphyry, and granodiorite are the main country rocks at the GKZ prospect. Thus, it is suggested that the IOCG at the SGUM and GKZ prospects are formed from one or more hydrothermal fluids associated with intermediate to felsic magmas. The upward migra-

tion of the mineralized fluids was facilitated by the presence of multiple shear zones that traversed the country rocks.

9. Conclusions

Detailed field, petrographical, and geochemical studies have revealed that gold and copper mineralizations are hosted by dacite and monzo- and syenogranite at the SGUM prospect and by diorite, granodiorite, and quartz-feldspar porphyry at the GKZ prospect. The country rocks are hydrothermally altered (albitization, sericitization, silicification, epidotization, and chloritization) and emplaced from a peraluminous to metaluminous calc-alkaline magma that has an island arc geochemical signature. The gold and copper mineralizations are confined to structurally controlled shear zones that were lately filled with auriferous quartz veins and alteration zones. All of the observed old trenches and shear zones at the GKZ prospect trended mainly in a NW–SE direction whereas NE–SW and NW–SE are the most dominant trends at the SGUM prospect. Evidence of shearing ranges from megascopic conjugate fractures and shear planes in the host rocks to microscopic sheared and crumbled Au-Cu ore assemblages. On the basis of the ore microscopy and EDX analyses, it seems that the alteration zones at the study areas were mainly composed of barite, oxide, and sulfide minerals. Oxides are represented by hematite (specularite) and magnetite. Specularite is formed due to the shearing of magnetite. All Fe-Cu sulfides post-date the formation of oxides. Secondary copper oxides and copper silicate minerals, in addition to native and electrum gold, were formed due to the hydration of Fe-Cu sulfides. The fire assay data of the alteration zone confirmed the presence of possibly sustainable gold up to 3.3. g/t, and the spot analyses indicated an electrum composition ($Au_{74.5-76.8}$ $Ag_{22.2-24.5}$). The gold contents in the alteration zones and quartz veins are promising for future gold exploitation and production in both the SGUM and GKZ prospects. The combined data in the present study show similarities in the style of mineralization at the SGUM and GKZ prospects with the IOCG deposits elsewhere in the ANS and other examples around the world.

References

1. Stern, R.J. Arc assembly and continental collision in the Neoproterozoic East African orogen: Implications for the consolidation of Gondwanaland. *Annu. Rev. Earth Planet. Sci.* **1994**, *22*, 319–351. [CrossRef]
2. Johnson, P.R.; Andresen, A.; Collins, A.S.; Fowler, A.R.; Fritz, H.; Ghebreab, W.; Kusky, T.; Stern, R.J. Late Cryogenian–Ediacaran history of the Arabian–Nubian Shield: A review of depositional, plutonic, structural, and tectonic events in the closing stages of the northern East African Orogen. *J. Afr. Earth Sci.* **2011**, *61*, 167–232.
3. Klemm, R.; Klemm, D.; Murr, A. Gold of the Pharaohs—6000 years of gold mining in Egypt and Nubia. *J. Afr. Earth Sci.* **2001**, *33*, 643–659. [CrossRef]
4. Botros, N.S. A new classification of the gold deposits of Egypt. *Ore Geol. Rev.* **2004**, *25*, 1–37.
5. Botros, N.S. Gold in Egypt does the future get worse or better? *Ore Geol. Rev.* **2015**, *67*, 189–207. [CrossRef]
6. Zoheir, B.A.; Johnson, P.R.; Goldfarb, R.J.; Klemm, D.D. Orogenic gold in the Egyptian Eastern Desert: Widespread gold mineralization in the late stages of Neoproterozoic orogeny. *Gond. Res.* **2019**, *75*, 184–217.
7. Harraz, H.Z.; Ashmawy, M.H. Structural and lithogeochemical cpnstraints on the localization of gold deposits at the El Sid-Fawakhir gold mine area, Eastern Desert, Egypt. *Egypt. J. Geol.* **1994**, *38*, 629.
8. Helmy, M.; Reinhard, K.; Fritz, H.; Loizenbauer, J. The Sukari Gold Mine, Eastern Desert-Egypt: Structural setting, mineralogy and fluid inclusion study. *Miner. Depos.* **2004**, *39*, 495–511. [CrossRef]
9. El Ramly, M.F. Geology and structures; General View of the Mineral Potential of Egypt. *Ann. Geol. Surv. Egypt.* **1970**, *1*, 46–53.
10. Takla, M.A. Economic potentialities of the shield and Phanerozoic rocks of Egypt. In Proceedings of the 6th International Conference on the Geology of Arab World, Cairo, Egypt, 21–24 February 2002; pp. 32–33.
11. Surour, A.A.; Attawiya, M.Y.; Hussein, H.A.; El-Feky, M.G. Shear zone microfabrics and multiple source of gold at the Hangaliya Mine, Eastern Desert, Egypt. *J. Geol.* **1999**, *43*, 39–52.
12. Obeid, M.A.; Jussein, A.M.; Abdallah, M.A. Shear zone-hosted gold mineralization in the Late Proterozic rocks of El Beida area, south Eastern Desert, Egypt. *Trans. Inst. Min. Metall. Sect. B Appl. Earth Sci.* **2001**, *110*, 192–204.
13. Surour, A.A.; El-Bayoumi, R.M.; Attawiya, M.Y.; El-Feky, M.G. Geochemistry of wall rock alterations and radioactive mineralization in the vicinity of Hangaliya uraniferous shear zone, Eastern Desert, Egypt. *Egypt. J. Geol.* **2001**, *45*, 187–212.
14. Zoheir, B.A. Characteristics and genesis of shear zone-related gold mineralization in Egypt: A case study from the Um El Tuyor mine, south Eastern Desert. *Ore Geol. Rev.* **2008**, *34*, 445–470. [CrossRef]
15. Surour, A.; Bakhsh, R. Microfabrics and microchemistry of sulfide ores from the 640 FEW level at the Al Amar gold mine, Saudi Arabia. *J. Microsc. Ultrastruct.* **2013**, *1*, 96–110. [CrossRef]
16. Surour, A.A.; Harbi, H.M.; Ahmed, A.H. The Bi'r Tawilah deposit, central western Saudi Arabia: Supergene enrichment of a Pan-African gold mineralization. *J. Afr. Earth Sci.* **2014**, *89*, 149–163. [CrossRef]
17. Abdelnasser, A.; Kumral, M.; Zoheir, B.; Karaman, M. REE geochemical char- acteristics and satellite-based mapping of hydrothermal alteration in Atud gold deposit, Egypt. *J. Afr. Earth Sci.* **2018**, *145*, 317–330. [CrossRef]
18. Surour, A.A.; Harbi, H.M.; Al-Sulbi, I. Mineralogical and geochemical characteristics of gold-hosted alteration zones in the Neoproterozoic arc metavolcanics at the Jabal Umm Watirah area, southwestern Saudi Arabia. *Arab. J. Geosci.* **2021**, *14*, 731. [CrossRef]
19. Hilmy, M.E.; Osman, A. Remobilisation of gold from a chalcopyrite–pyrite mineralisation Hamash gold mine, Southeastern Desert, Egypt. *Miner. Depos.* **1989**, *24*, 244–249. [CrossRef]
20. Hussein, A.A. Mineral deposits. In *The Geology of Egypt*; Said, R., Ed.; Routledge: London, UK, 1990; pp. 511–566.
21. Botros, N.; Wetait, M. Possible porphyry copper mineralization in south Um Monqul, Eastern Desert, Egypt. *Egypt. J. Geol.* **1997**, *41*, 175–196.
22. Helmy, H.M.; Kaindl, R. Mineralogy and fluid inclusion studies of the Au-Cu quartz veins in the Hamash area, South-Eastern Desert, Egypt. *Mineral. Petrol.* **1999**, *65*, 69–86. [CrossRef]
23. Salem, S.M.; Arafa, S.A.; Ramadan, T.M.; El Gammal, E.A. Exploration of copper deposits in Wadi El Regeita area, Southern Sinai, Egypt, with contribution of remote sensing and geophysical data. *Arab. J. Geosci.* **2013**, *6*, 321–335. [CrossRef]
24. Mamedov, E.A.; Ahmed, E.S.; Chiragov, M.I. Copper–gold–sulfide mineralization associated with late Precambrian volcanic ring structures, southern Sinai, Egypt. *Arab. J. Sci. Eng.* **2014**, *39*, 273–286. [CrossRef]
25. Ahmed, A.H.; Gharib, M.E. Porphyry Cu mineralization in the eastern desert of Egypt: Inference from geochemistry, alteration zones, and ore mineralogy. *Arab. J. Geosci.* **2016**, *9*, 179–205. [CrossRef]
26. Bierlein, F.P.; Reynolds, N.; Arne, D.C.; Bargmann, C.J.; McKeag, S.; Bullen, W.; Al Athbah, H.; McKnight, S.; Maas, R. Petrogenesis of a Neoproterozoic magmatic arc hosting porphyry Cu-Au mineralization at Jebel Ohier in the Gebeit Terrane, NE Sudan. *Ore Geol. Rev.* **2016**, *79*, 133–154. [CrossRef]
27. Abd El-Rahman, Y.; Seifert, T.; Said, A. The South Um Mongul Cu-Mo-Au prospect in the northern Eastern Desert of Egypt: Tonian porphyry-style mineralization with an Ediacaran hydrothermal iron oxide overprint. *Ore Geol. Rev.* **2018**, *99*, 217–234. [CrossRef]
28. Hitzman, M.W.; Oreskes, N.; Einaudi, M.T. Geological characteristics and tectonic setting of Proterozoic iron oxide (Cu–U–Au–REE) deposit. *Precamb. Res.* **1992**, *58*, 241–287. [CrossRef]
29. Kerrich, R.; Goldfarb, R.; Groves, D.I.; Garwin, S. The geodynamics of world-class gold deposits: Characteristics, space–time distribution, and origins. *Rev. Econ. Geol.* **2000**, *13*, 501–551.

30. Hitzman, M.W.; Valenta, R.K. Uranium in iron oxide-copper–gold (IOCG) systems. *Econ. Geol.* **2005**, *100*, 1657–1661. [CrossRef]

31. Williams, P.J.; Barton, M.D.; Fontboté, L.; de Haller, A.; Johnson, D.A.; Mark, G.; Marschik, R.; Oliver, N.H.S. Iron-oxide-copper-gold deposits: Geology, space-time distribution, and possible modes of origin. In *Economic Geology 100th Anniversary*; Society of Economic Geologists, Thee University of Texas at Austin: Austin, TX, USA, 2005; pp. 371–406.

32. Foster, A.R.; Williams, P.J.; Ryan, C.G. Distribution of gold in hypogene ore at the Ernest Henry iron oxide copper-gold deposit, Cloncurry district, NW Queensland. *Explor. Min. Geol.* **2007**, *16*, 125–143. [CrossRef]

33. Frimmel, H.E. Earth's continental crustal gold endowment. *Earth Planet. Sci. Lett.* **2008**, *267*, 45–55. [CrossRef]

34. Groves, D.I.; Bierlein, F.P.; Meinert, L.D.; Hitzman, M.W. Iron oxide copper–gold (IOCG) deposits through Earth history: Implications for origin, lithospheric setting, and distinction from other epigenetic iron oxide deposits. *Econ. Geol.* **2010**, *105*, 641–654. [CrossRef]

35. Porter, T.M. Advances in the Understanding of IOCG and Related Deposits. In *Hydrothermal Iron Oxide Copper–Gold and Related Deposits*; Porter, T.M., Ed.; A Global Perspective V3; PGC Publishing: Adelaide, Australia, 2010; pp. 5–106.

36. Chen, H. External sulphur in IOCG mineralization: Implications on definition and classification of the IOCG clan. *Ore Geol. Rev.* **2013**, *51*, 74–78. [CrossRef]

37. Doebrich, J.L.; Al-Jehani, A.M.; Siddiqui, A.A.; Hayes, T.S.; Wooden, J.L.; Johnson, P.R. Geology and metallogeny of the Ar Rayan terrane, eastern Arabian shield: Evolution of a Neoproterozoic continental-margin arc during assembly of Gondwana within the East African Orogen. *Precamb. Res.* **2007**, *158*, 17–50. [CrossRef]

38. Fletcher, R.J. *NI 43-101 Technical Report on the Um Balad/ElUrf Exploration Concession Area in Egypt*; Behre Dolbear Project Number J09-107; SMW Gold Limited: Cairo, Egypt, 2009.

39. Tawab, M.A.; Castel, G.; Pouit, G.; Ballet, P. Archéo-géologie des ancienne mines de cuivre et d'or des régions El-Urf/Mongul-Sud et Dara Ouest. *Bull. L'inst. Fr. D'Archéol. Orient.* **1990**, *90*, 359–364.

40. Osman, A. *Native Gold Mineralization Associated with Iron Oxides, Mongul Area, Northern Eastern Desert, Egypt*; Earth Science Series; Middle East Research Center, Ain Shams University: Cairo, Egypt, 1994; pp. 74–87.

41. EMRA. *Geological and Geochemical Exploration of Gold and Copper Deposits in Basement Rocks at Wadi Dara and in Sedimentary Rocks at Wadi Araba, North Eastern Desert, Egypt*; Internal Report (expedition No. G2-2013); Exploration Department, The Egyptian Mineral Resources Authority: Cairo, Egypt, 2013; p. 124.

42. Eliwa, H.; Breitkreuz, C.; Murata, M.; Khalaf, I.; Bühler, B.; Itaya, T.; Takahashi, T.; Hirahara, Y.; Miyazaki, T.; Kimura, J. SIMS zircon U–Pb and mica K–Ar geochronology, and Sr–Nd isotope geochemistry of Neoproterozoic granitoids and their bearing on the evolution of the north Eastern Desert, Egypt. *Gond. Res.* **2014**, *25*, 1570–1598. [CrossRef]

43. Breitkreuz, C.; Eliwa, H.; Khalaf, I.; El Gameel, K.; Bühler, B.; Sergeev, S. Neoproterozoic SHRIMP U–Pb zircon ages of silica-rich dokhan volcanics in the North Eastern Desert, Egypt. *Precamb. Res.* **2010**, *182*, 163–174. [CrossRef]

44. Azzaz, S.A.; Kharbish, S.; El-Alfy, H.M. Geological and geochemical investigations on Hammamat molasse sediments, G. Kharaza, Eastern Desert, Egypt. *Acta Univ. Matthiae Belii Ser. Environ. Manazerstov.* **2015**, *2*, 7–28.

45. Abd El-Rahman, Y.; Seifert, T.; Gutzmer, J.; Said, A.; Hofmann, M.; Gärtner, A.; Linnemann, U. The South Um Mongul Cu-Mo-Au prospect in the Eastern Desert of Egypt: From a mid-Cryogenian continental arc to Ediacaran post-collisional appinite-high Ba-Sr monzogranite. *Ore Geol. Rev.* **2017**, *80*, 250–266. [CrossRef]

46. El-Desoky, H.M.; Hafez, H.M. Petrology, Geochemistry and Mineralogy of the Hydrothermally Altered Rock Units at Wadi Dara, North Eastern Desert, Egypt. *Ann. Geol. Surv. Egypt* **2018**, *35*, 103–140.

47. Chen, Z.; Zeng, Z.; Wang, X.; Yin, X.; Chen, S.; Guo, K.; Wu, L. U-Th/He dating and chemical compositions of apatite in the dacite from the southwestern Okinawa Trough: Implications for petrogenesis. *J. Asian Earth Sci.* **2018**, *161*, 1–13. [CrossRef]

48. Deer, W.A.; Howie, A.; Zussman, J. *An Introduction to Rock-Forming Minerals*; 17th Longman Ltd.: London, UK, 1986; Volume 51, p. 629.

49. Nachit, H.; Ibhi, A.; Ohoud, M.B. Discrimination between primary magmatic biotites, reequilibrated biotites and neoformed biotites. *C. R. Geosci.* **2005**, *337*, 1415–1420. [CrossRef]

50. Abdel-Rahman, A.F.M. Nature of biotites from alkaline, calc-alkaline, and peraluminous magmas. *J. Petrol.* **1994**, *35*, 525–541. [CrossRef]

51. Henry, D.J.; Guidotti, C.V.; Thomson, J.A. The Ti-saturation surface for low-to-medium pressure metapelitic biotites: Implications for geothermometry and Ti-substitution mechanisms. *Am. Mineral.* **2005**, *90*, 316–328. [CrossRef]

52. Morimoto, N.; Fabries, J.; Ferguson, A.K.; Ginzburg, I.V.; Ross, M.; Seifert, F.A.; Gottardi, G. Nomenclature of pyroxenes. *Mineral. Mag.* **1988**, *52*, 535–550. [CrossRef]

53. Hey, M.H. A new review of the chlorites. *Mineral. Mag.* **1954**, *30*, 277–292. [CrossRef]

54. Leake, B.E.; Woolley, A.R.; Arps, C.E.; Birch, W.D.; Gilbert, M.C.; Grice, J.D.; Youzhi, G. Nomenclature of amphiboles report; of the subcommittee on amphiboles of the International Mineralogical Association, Commission on New Minerals and Mineral Names. *Can. Mineral.* **1997**, *35*, 219–246.

55. Pe-Piper, G. Relationship of amphibole composition to host-rock geochemistry: The A-type gabbro-granite Wentworth pluton, Cobequid shear zone, eastern Canada. *Eur. J. Mineral.* **2007**, *19*, 29–38. [CrossRef]

56. Deer, W.A.; Howie, R.A.; Zussman, J. *An Introduction to the Rock Forming Minerals*, 2nd ed.; Longman Scientific and Technical: London, UK, 1992; Volume 696.

57. Cox, K.G.; Bell, J.D.; Pankhurst, R.J. *The Interpretation of the Igneous Rocks*; George Allen and Unwin: London, UK, 1979; Volume 450.

58. Winchester, J.A.; Floyd, P.A. Geochemical discrimination of different magma series and their differentiation products using immobile elements. *Chem. Geol.* **1977**, *20*, 323–343. [CrossRef]

59. Middlemost, E.A.K. Naming materials in the magma/igneous rock system. *Earth Sci. Rev.* **1994**, *37*, 215–244. [CrossRef]

60. Irvine, T.N.; Baragar, W.R.A. A guide to the chemical classification of the common volcanic rocks. *Can. J. Earth Sci.* **1971**, *8*, 523–548. [CrossRef]

61. Ali, K.A.; Moghazi, A.K.M.; Maurice, A.E.; Omar, S.A.; Wang, Q.; Wilde, S.A.; Moussa, E.M.; Manton, W.I.; Stern, R.J. Composition, age, and origin of the ~620 Ma Humr Akarim and Humrat Mukbid A-type granites: No evidence for pre-Neoproterozoic basement in the Eastern Desert, Egypt. *Int. J. Earth Sci.* **2012**, *101*, 1705–1722. [CrossRef]

62. Maniar, P.D.; Piccoli, P.M. Tectonic discrimination of granitoids. *Geol. Soc. Am. Bull.* **1989**, *101*, 635–643. [CrossRef]

63. Peccerillo, A.; and Taylor, S.R. Geochemistry of Eocene calc-alkaline volcanic rocks from the Kastamonu area, northern Turkey. *Contrib. Mineral. Petrol.* **1976**, *58*, 63–81. [CrossRef]

64. Woodhead, J.; Eggins, S.; Gamble, J. High field strength and transition element systematics in island and back-arc basin basalts: Evidence for multi-phase extraction and a depleted mantle wedge. *Earth Planet. Sci. Lett.* **1993**, *114*, 491–504. [CrossRef]

65. Annen, C.; Bluny, J.D.; Sparks, R.S.J. The genesis of intermediate and silicic magmas in deep crustal hot zone. *J. Petrol.* **2006**, *47*, 505–539. [CrossRef]

66. Roberts, M.P.; Clemens, J.D. Origin of high-potassium, calc-alkaline, I-type granitoids. *Geology* **1993**, *21*, 825–828. [CrossRef]

67. Fowler, M.B.; Kocks, H.; Darbyshire, D.P.F.; Greenwood, P.B. Petrogenesis of high Ba–Sr plutons from the Northern Highlands Terrane of the British Caledonian Province. *Lithos* **2008**, *105*, 129–148. [CrossRef]

68. Peccerillo, A.; Barberio, M.R.; Yirgu, G.; Ayalew, D.; Barbieri, M.; Wu, T.W. Relationships between mafic and peralkaline silicic magmatism in continental rift settings: A petrological, geochemical and isotopic study of the Gedemsa Volcano, Central Ethiopian Rift. *J. Petrol.* **2003**, *44*, 2003–2032. [CrossRef]

69. Ye, H.M.; Li, X.H.; Li, Z.X.; Zhang, C.L. Age and origin of high Ba–Sr appinitegranites at the northwestern margin of the Tibet Plateau: Implications for early Paleozoic tectonic evolution of the Western Kunlun orogenic belt. *Gond. Res.* **2008**, *13*, 126–138. [CrossRef]

70. Patiño Douce, A.E. What do experiments tell us about the relative contributions of crustal and mantle to the origin of granitic magmas? In *Understanding Granites: Intergrating New and Classical Techniques*; Castro, A., Fernández, C., Vigneresse, J.L., Eds.; Geological Society, Special Publication: London, UK, 1999; Volume 168, pp. 55–75.

71. Muir, R.J.; Weaver, S.D.; Bradshaw, J.D.; Eby, G.N.; Evans, J.A. The Cretaceous Separation Point batholith, New Zealand: Granitoid magmas formed by melting of mafic lithosphere. *J. Geol. Soc. Lond.* **1995**, *152*, 689–701. [CrossRef]

72. Twist, D.; Harmer, R.E.J. Geochemistry of contrasting siliceous magmatic suites in the Bushveld Complex: Genetic aspects and implications for tectonic discrimination diagrams. *J. Volcanol. Geotherm. Res.* **1987**, *32*, 83–98. [CrossRef]

73. Stern, R.J.; Gottfried, D.; Hedge, C.E. Late Precambrian rifting and crustal evolution in the North Eastern Desert of Egypt. *Geology* **1984**, *12*, 168–172. [CrossRef]

74. Willis, K.M.; Stern, R.J.; Clauer, N. Age and geochemistry of Late Precambrian sediments of the Hammamat sediments from the northeastern Desert of Egypt. *Precamb. Res.* **1988**, *42*, 173–187. [CrossRef]

75. Spandler, C.; Pirard, C. Element recycling from subducting slabs to arc crust: A review. *Lithos* **2013**, *170*, 208–223. [CrossRef]

76. Pearce, J.A. Geochemical evidence for the genesis and eruptive setting of lava from Tethyan ophiolites. In *International Ophiolite Symposium*; Panayiotou, A., Ed.; Ministry of Agriculture and Mineral Resources, Geological Survey Department: Nicosia, Cyprus, 1980; pp. 261–272.

77. Defant, M.J.; Drummond, M.S. Derivation of some modern arc magmas by melting of young subducted oceanic lithosphere. *Nature* **1990**, *347*, 662–665. [CrossRef]

78. Muller, D.; Rock, N.M.S.; Groves, D.I. Geochemical discrimination between shoshonitic and potassic volcanic rocks in different tectonic settings: A pilot study. *Mineral. Petrol.* **1992**, *46*, 259–289. [CrossRef]

79. Condie, K.C.; Kröner, A. The building blocks of continental crust: Evidence from a major change in the tectonic setting of continental growth at the end of the Archean. *Gond. Res.* **2013**, *23*, 394–402. [CrossRef]

80. Pitcher, W.S. Granite and yet more granites forty years on. *Geol. Rundsch.* **1987**, *76*, 51–79. [CrossRef]

81. Pearce, J.A.; Harris, N.B.W.; Tindle, A.G. Trace Element Discrimination Diagrams for the Tectonic Interpretation of Granitic Rocks. *J. Petrol.* **1984**, *25*, 956–983. [CrossRef]

82. Khedr, M.Z.; Abo Khashaba, S.M.; El-Shibiny, N.H.; El-Arafy, R.A.; Takazawa, E.; Azer, M.K.; Palin, R.M. Remote sensing techniques and geochemical constraints on the formation of the Wadi El-Hima mineralized granites, Egypt: New insights into the genesis and accumulation of garnets. *Int. J. Earth Sci.* **2022**, *111*, 2409–2443. [CrossRef]

83. Bühler, B.; Breitkreuz, C.; Pfänder, J.A.; Hofmann, M.; Becker, S.; Linnemann, U.; Eliwa, H.A. New insights into the accretion of the Arabian–Nubian Shield: Depositional setting, composition and geochronology of a mid-Cryogenian arc succession (North Eastern Desert, Egypt). *Precamb. Res.* **2014**, *243*, 149–167. [CrossRef]

84. Wang, Y.H.; Xue, C.J.; Liu, J.J.; Wang, J.P.; Yang, J.T.; Zhang, F.F.; Zhao, Z.N.; Zhao, Y.J.; Liu, B. Early Carboniferous adakitic rocks in the area of the Tuwu deposit, eastern Tianshan, NW China: Slab melting and implications for porphyry copper mineralization. *J. Asian Earth Sci.* **2015**, *103*, 332–349. [CrossRef]

85. Zhang, F.F.; Wang, Y.H.; Liu, J.J.; Xue, C.J.; Wang, J.P.; Zhang, W.; Yan, L.L. Paleozoic magmatism and mineralization potential of the Sanchakou copper deposit, Eastern Tianshan, Northwest China: Insights from geochronology, mineral chemistry, and isotopes. *Econ. Geol.* **2022**, *117*, 165–194. [CrossRef]

86. Hitzman, M.W. Iron oxide-Cu-Au deposits: What, where, when, and why. In *Hydrothermal Iron Oxide Copper-Gold and Related Deposits*; Porter, T.M., Ed.; A Global Perspective V2; PGC Publishing: Adelaide, Australia, 2000; pp. 9–26.

87. Sillitoe, R.H. Iron oxide-copper-gold deposits: An Andean view. *Miner. Depos.* **2003**, *38*, 787–812. [CrossRef]

88. Barton, M.D. Iron oxide(-Cu–Au–REE–P–Ag–U–Co) systems. 2nd edition. *Treatise Geochem.* **2014**, *13*, 515–541.

89. Skirrow, R.G. Iron oxide copper-gold (IOCG) deposits–A review (part 1): Settings, mineralogy, ore geochemistry and classification. *Ore Geol. Rev.* **2022**, *140*, 104–569. [CrossRef]

90. Monteiro, L.V.; Xavier, R.P.; de Carvalho, E.R.; Hitzman, M.W.; Johnson, C.A.; de Souza Filho, C.R.; Torresi, I. Spatial and temporal zoning of hydrothermal alteration and mineralization in the Sossego iron oxide–copper–gold deposit, Carajás Mineral Province, Brazil: Paragenesis and stable isotope constraints. *Miner. Depos.* **2008**, *43*, 129–159. [CrossRef]

91. Richards, J.P.; Mumin, A.H. Magmatic–hydrothermal processes within an evolving Earth: Iron oxide-copper–gold and porphyry Cu ± Mo ± Au deposits. *Geology* **2013**, *41*, 767–770. [CrossRef]

92. Uvarova, Y.A.; Pearce, M.A.; Liu, W.; Cleverley, J.S. Geochemical Signature of Copper Redistribution in IOCG-type Mineralization. Gawler Craton, South Australia. *Miner. Depos.* **2017**, *53*, 477–492. [CrossRef]

93. Rotherham, J.F. A metasomatic origin for the iron-oxide Au–Cu Starra orebodies, eastern fold belt, Mount Isa Inlier. *Miner. Depos.* **1997**, *32*, 205–218. [CrossRef]

94. Tazava, E.; de Oliveira, C.G. The Igarapé Bahia Au–Cu-(REE-U) deposit, CarajásMineral Province, Northern Brazil. In *Hydrothermal Iron Oxide Copper–Gold and Related Deposits*; Porter, T.M., Ed.; A Global Perspective V3; PGC Publishing: Adelaide, Australia, 2000; pp. 203–212.

95. Sun, Y.; Li, C.D.; Feng, Z.J. A study of the gold content and occurrence of Lala copper ore deposit in Sichuan province. *J. Mineral. Petrol.* **1994**, *14*, 67–73.

96. Goad, R.E.; Mumin, A.H.; Duke, N.A.; Neale, K.L.; Mulligan, D.L. Geology of the Proterozoic iron oxide-hosted, NICO cobalt–gold–bismuth, and Sue-Dianne copper–silver deposits, southern Great Bear magmatic zone, Northwest Territories, Canada. In *Hydrothermal Iron Oxide Copper–Gold and Related Deposits*; Porter, T.M., Ed.; A Global Perspective V3; PGC Publishing: Adelaide, Australia, 2000; pp. 249–267.

97. Strickland, C.D.; Martyn, J.E. The Guelb Moghrein Fe-oxide copper–gold–cobalt deposit and associated mineral occurrences, Mauritania: A geological introduction. In *Hydrothermal Iron Oxide Copper–Gold and Related Deposits*; Porter, T.M., Ed.; A Global Perspective V2; PGC Publishing: Adelaide, Australia, 2001; pp. 275–291.

98. McLean, R.N. The Sin Quyen iron oxide–copper–gold–rare earth oxide mineralisation of North Vietnam. In *Hydrothermal Iron Oxide and Copper–Gold Related Deposits*; Porter, T.M., Ed.; A Global Perspective V2; PGC Publishing: Adelaide, Australia, 2001; pp. 293–301.

99. Sleigh, D.W.W. The Selwyn line tabular iron–copper–gold system, Mount Isa Inlier, NW Queensland, Australia. In *Hydrothermal Iron Oxide Copper–Gold and Related Deposits*; Porter, T.M., Ed.; A Global Perspective V2; PGC Publishing: Adelaide, Australia, 2002; pp. 77–93.

100. Rusk, B.G.; Oliver, N.H.S.; Cleverley, J.S.; Blenkinsop, T.G.; Zhang, D.; Williams, P.J.; Habermann, P. Physical and chemical characteristics of the Ernest Henry Iron Oxide copper gold deposit, Australia; implications for IOCG genesis. In *Hydrothermal Iron Oxide Copper–Gold and Related Deposits*; Porter, T.M., Ed.; A Global Perspective V2; PGC Publishing: Adelaide, Australia, 2010; pp. 201–218.